Representative elementary volumes, hysteresis and heterogeneity in multiphase flow from the pore to continuum scale

Samuel J. Jackson
Department of Earth Science & Engineering
Imperial College London
London, U.K.
samuel.jackson@imperial.ac.uk

Qingyang Lin
Department of Earth Science & Engineering
Imperial College London
London, U.K.
q.lin11@imperial.ac.uk

Samuel Krevor
Department of Earth Science & Engineering
Imperial College London
London, U.K.
s.krevor@imperial.ac.uk

September 21, 2019

Abstract

In this work, we use a multi-scale experimental and modelling approach to address fundamental, unanswered questions relating pore-scale fluid dynamics and their upscaled, continuum representation in subsurface multiphase flow. We utilise core flooding experiments with micro X-Ray CT imaging to analyse the role of representative elementary volumes (REVs), hysteresis and heterogeneity in multiphase flow in two distinct water-wetting Bentheimer sandstone samples. Experimental observations resolve the pore space at 6μm across a field of view up to 12 $\times$ 12 $\times$ 65mm with simultaneous measurements of differential pressure during fluid flow. The REV for both porosity and capillary pressure is approximately 2mm for both samples. In contrast, due to capillary pressure heterogeneities, the REV for saturation exceeds 8mm, the largest scale investigated. Predictions of fluid connectivity and hysteresis during imbibition using the Land trapping model are validated; fluid connectivity can be used to predict imbibition flow properties in homogenous media. However, fluid connectivity is also influenced by heterogeneities at scales larger than the REV. Both pore- and continuum-scale fluid connectivity must be accounted for in models of upscaled flow properties. The complex interplay of pore accessibility, availability and snap-off in heterogeneous media plays a crucial role in controlling connectivity and trapping at the continuum scale. We develop a hysteretic, 3D numerical model with REV scale heterogeneities, which is largely able to predict the impacts of these multi-modal heterogeneities in low capillary number multiphase flow. The experimental dataset herein provides an excellent benchmark for future development of continuum scale modelling frameworks.

1 Introduction

In order to tractably model large scale subsurface fluid flow, the porous rock-fluid system is treated as a continuum [1]. The prevailing continuum framework makes use of Darcy's law, and defines macroscopic properties - porosity, permeability, saturation, capillary pressure, relative permeability and trapping, which defines hysteresis in the properties. These properties represent the aggregate behaviour of fluids moving through a capillary network formed by the pores and fractures of the rock strata. The approach underpins commercial oil and gas production [2], groundwater management [3], the cleanup of subsurface contaminants radioactive waste and NAPL [4, 5], and the large scale mitigation of climate change through subsurface CO_2 storage [6].

With respect to two phase fluid flow, there remain a number of outstanding questions about the relationship between the fluid dynamics within the pores of the rocks and their upscaled, continuum scale, manifestation. The continuum approach relies on the concept of a representative elementary volume, or REV. While the REV for porosity and permeability has been exhaustively studied (see for example [7–10]), the REV for multiphase flow properties, relative permeability and capillary pressure is not understood [11]. Similarly, pore-scale fluid morphology has long been invoked as the underlying cause for hysteresis in continuum properties of relative permeability and capillary pressure [12–15]. One of the earliest and most widely used trapping models, the Land model, correlates hysteresis with the fraction of fluid phase that is connected vs. isolated as residually trapped ganglia within the pores [12]. While the model fits well to observations in cm-scale rock cores, the validity of its pore-scale conceptual picture is undetermined. Finally, the continuum properties of rock systems are typically measured on rock cores of length scale 10 cm - 1m. However, heterogeneity in continuum properties at scales even smaller than the rock cores can, and perhaps usually do, place leading order controls on flow with field scale manifestations [16–22]. There is no consensus on the extent to which heterogeneity in multiphase flow properties at these small scales must be accounted for in upscaled models.

The major obstacle to answering these questions has been in the difficulty in observing small scale fluid displacement and distribution in rocks simultaneous with the measurement of continuum scale properties. Even with the recent availability of laboratory and synchrotron X-ray CT direct links between pore-scale fluid properties and their continuum manifestations are challenging [23]. They require a combination of imagery at a spatial resolution of micrometres simultaneous with measurements across samples of cm-scale dimensions. There are direct trade-offs inherent in the physics of X-ray CT between field of view and spatial resolution. As a result, few studies have measured pore-scale properties simultaneous with, e.g., relative permeability. Notably [24, 25] have measured relative permeability and capillary pressure simultaneous with a resolution of the pore-scale fluid distribution, demonstrating the potential of this approach.

In this work, we address the challenges in linking pore-scale fluid dynamics with their continuum manifestations with a multi-scale experimental and modelling approach. We perform steady-state drainage and imbibition core flooding experiments in two distinct, *cm-scale* Bentheimer cores with detailed X-Ray CT imaging and simultaneous differential pressure measurements. We use a homogeneous and a layered heterogeneous Bentheimer sandstone core to study, and decouple the impacts of REV, hysteresis and heterogeneity in multiphase flow. The sample size is optimised to allow micron level micro-CT imaging across hundreds of REVs. The interfaces between fluid phases and their connectivity through individual pores can be resolved, whilst allowing the determination of continuum scale multiphase flow properties - relative permeability, capillary pressure and trapping. Imaging methods, analysis and modelling from both pore and continuum scales are applied simultaneously on the same core, allowing the inclusion of complimentary information.

The experimental data is used to develop hysteretic, 3D continuum scale numerical models of the homogeneous and heterogeneous Bentheimer sandstone samples. We make use of the high resolution imagery and differential pressure measurements in the experiments to evaluate some of the base assumptions in the conceptual picture underpinning of these continuum models, evaluating (1) the representative elementary volume for single and multiphase flow properties, (2) the relationship between hysteresis and connected fluid phase saturations (3) the link between heterogeneity in capillary pressure characteristics and the impact on average flow, and flow properties, across the scales at which measurements would typically be obtained. In this way, the continuum scale models are directly validated and compared with pore- and continuum-scale information in a multi-scale analysis.

In the following, we first outline the experimental methods used to obtain the observations. Subsequently we present the theoretical and numerical modelling framework used in the study. Experimental results are then discussed followed by numerical modelling, directly evaluating the key points above.

2 Experimental methods

2.1 Core flooding

We perform steady-state core flooding experiments with micro-CT imaging on two Bentheimer sandstone cores of diameter 12.35mm (cored with a 12.7mm, $1/2$" drill bit), and length 73.2mm and 64.7mm, with core-averged porosities of 0.203 and 0.223 respectively. The shallow-marine Bentheimer sandstone typically consists of around 95% quartz with minor feldspar and clay and has a well-sorted grain size distribution [26].

Typical core samples used for multiphase flow experiments are shown in Figure 1a, with the cm-scale core used in this experimental campaign shown in the centre. Millimetre-scale cores are typically used for pore-scale flow experiments, since they allow detailed micro-CT imaging at resolutions of 1-4 microns [27, 28], imaging volumes typically around 1-100mm^3. For Bentheimer sandstones, the representative elementary volumes (REV) for porosity is typically between

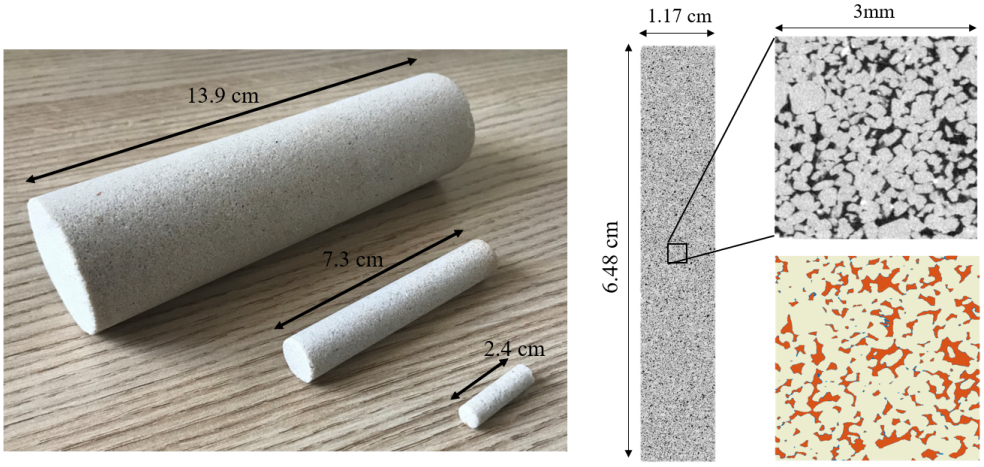

(a) (b)

Figure 1: (a) Typical X-Ray CT-Core flooding samples sizes (Bentheime cores). The smallest mm-scale cores typically have diameters of 4-6mm. The largest macro cores typically have diameters of 35-65mm. The cm-scale core (middle) has dimensions in between that allow pore-scale imaging (i.e. $O(\mu m)$ resolution) across continuum scales (i.e. several REVs). (b) Raw, unfiltered Micro-CT image of the dry meso core from (a), showing raw and segmented zoomed in regions on the top and bottom respectively.

1 and 60 mm^3 [29, 30], but can be larger for flow dependent properties such as saturation [30]. This means that often an REV is often not reached on a mm-scale sample, and while these cores allow detailed investigations of pore-scale displacement mechanisms [31, 32], any upscaled, averaged flow properties are not representative of continuum scale flow, in which an REV defines the smallest averaging unit.

At larger scales, macroscopic cores (Figure 1a top) are often used in special core analysis experiments [33], and allow the derivation of continuum scale flow properties. With the inclusion of REV scale structural heterogeneity, intrinsic multiphase flow properties can be found obtained even in highly heterogeneous samples [22]. However, in these approaches, pore-scale features and displacement mechanisms cannot be directly visualised, which hinders continuum scale model development; unvalidated assumptions often have to be made on the multiphase flow regime, i.e. connected pathway flow, capillary equilibrium and trapping evolution.

In this work, the sample size is optimised to allow detailed micron level micro-CT imaging across hundreds of REVs. The Bentheimer samples in this study have permeabilities of 1.636D $\pm$ 0.025D and 0.681D $\pm$ 0.006D respectively, average pore diameters of $\approx 80\mu$m [26] and volumes of 8769mm^3 and 7750mm^3 respectively. Using a full core scan resolution of 6μm means that the fluid phases in individual pores can be resolved, whilst allowing 100s of REVs to be imaged. Imaging methods, analysis and modelling from both pore and continuum scales can then be applied simultaneously on the same core, allowing the inclusion of complementary information.

In the core flooding experiments, brine (3.5wt.% KI) and decane (99.9% pure, Sigma-Aldrich) are used as wetting and non-wetting phases respectively, with an interfacial tension of $\approx$ 51.16 mN/m (for the pure DI water - decane system [34], with maximum $\pm$ 0.5 mN/m for the addition of small KI salt concentrations to the water [35]). The experimental pore pressure is maintained at 1.5MPa, and the temperature T at 30 °C (core 1 experiment, T = 30.11 °C $\pm$ 0.46 °C, core 2 experiment, T = 29.90 °C $\pm$ 0.44 °C. These conditions result in fluid viscosities for brine and decane as 7.83 $\times$ 10^{-4}Pa.s [36] and 8.03 $\times$ 10^{-4}Pa.s [37] respectively, and densities of 723.8kg.m^{-3} [38] and 1023.2kg.m^{-3} [37] respectively. These fluids are chosen for their relative stability in the core-flooding experiments (as opposed to gaseous flows) and their analogy to other immiscible fluid pairs found in subsurface flows, for example in carbon sequestration (supercritical CO_2-brine), oil recovery (Crude oil - brine) and contaminant transport (NaPLs - brine).

In order to assess the impact of structural heterogeneities at the pore and continuum scales, the cores are flooded at very low flow rates (total flow rate, Q_{tot} = 0.1 ml.min^{-1}), at near unity viscosity ratio ($\mu_{nw}/\mu_w = 1.025$). The pore-scale capillary number at the final fractional flow of oil during drainage $f_{nw} = 1$ is $N_{cp} = \frac{q\mu}{\sigma} = 2.4\text{x}10^{-7}$, where q is the Darcy velocity, μ is the invading phase dynamic viscosity and σ is the fluid-fluid interfacial tension. The macroscopic, continuum scale capillary at the same fractional flow is $N_{cm} = \frac{\Delta P}{L}\frac{H}{\Delta P_c} \approx 0.25$, where ΔP is the core-averaged pressure drop over length L and ΔP_c is the variation in characteristic capillary pressure over heterogeneity length scale H [39]. Here, ΔP_c is taken as 1.5 kPa [22], over a length scale H equal to the core radius. The macroscopic capillary

number indicates the flow is nearing the capillary limit, far below the transition to viscous-dominated flow reported typically in the range N_{cm} = 10-100 [22, 39]. Macroscopic structural heterogeneities will therefore dominate the flow regime, controlling the flow path and potential [40]. At the pore-scale, the flow is at capillary equilibrium and should exhibit a connected pathway flow regime [41], being below typical values reported for intermittent flow [24, 42–44] and ganglion dynamics [45]. This capillary number is of the same order of magnitude as previous experiments performed on Bentheimer mm-scale cores, allowing comparison with the pore-scale works of [25, 46].

The core flooding experimental procedure is detailed in the supporting information, and summarised here. We use a similar approach to that described in [25], optimised for a large sample size and core stability during long scans. The core is placed in the core-holder setup shown in SI Figure 1 with a confining pressure of 4.5MPa to prevent fluid-bypass between the core and viton sleeve. A full-core dry scan of the air-saturated core is first taken, using the imaging methodology described in section 2.2. The core is then saturated with high-salinity brine (30wt.% KI) by flowing at least 100 pore volumes through at high-flow rate (Q_{tot} = 5 ml.min^{-1}) with a back-pressure (pore-pressure) of 1.5MPa, to fully displace any air in the system. A full-core scan is then taken for the differential imaging procedure. The working fluid brine (3.5wt.% KI) is then pumped through the core, fully displacing the high-salinity brine, and the absolute permeability is measured. Following this, decane and brine are co-injected into the core at constant total flow rate varying the fractional flow in a drainage and imbibition process. At each fractional flow, once the differential pressure has stabilised across the core (typically once $\Delta P/\Delta t < 0.05$kPa.h^{-1}, or a minimum of 6 hours if this is achieved very quickly) a full-core scan is taken followed by zoom-in, region of interest scans. Graphs of the differential pressure through time for both cores are shown in the supporting information Figure 7.

2.2 X-Ray micro-CT imaging and processing

Once steady-state has been reached at each fractional flow a full core X-Ray micro-CT scan is taken using a flat panel detector in a Zeiss Versa 510 X-Ray microscope at a resolution of 6μm. Full details of the scanning and image processing can be found in the supporting information. In summary, 11 and 10 individual scans are taken at increasing vertical locations in each core, to cover a total volume after processing of 1950 $\times$ 1950 $\times$ 10800 voxels (11.7mm $\times$ 11.7mm $\times$ 64.8mm) and 1900 $\times$ 1900 $\times$ 9550 voxels (11.4mm $\times$ 11.4mm $\times$ 57.3mm) respectively. Approximately 5mm is lost from the images near the inlet and outlet of the core due to noise from the aluminium end-pieces and the cone angle of the X-Ray beam. There is significant overlap between each scan to allow registration and merging of the full image. Each individual scan image is normalised to pre-selected references to obtain consistent grey-scale values throughout the core, after which two weak non-local means filters are applied to the image for noise reduction [47]. Scanning of the full core takes approximately 11 hours.

After each full-core scan, a selection of zoom-in, region of interest scans are performed to facilitate the interfacial curvature measurements (discussed below). A 4x microscope objective lens is used to aquire each image, with the detector position varied to achieve a 3.5μm resolution and 2μm resolution image, each containing 1000 ^{3} voxels. These scans take 18hrs and 24hrs respectively.

After image acquisition and post-processing, the images are segmented. The full core dry and high-salinity brine images are used to accurately segment the pore space into micro and macro porous regions. The differential image (high-salinity - dry + constant) is globally thresholded using suitable grey-scale values to obtain regions of grain, macro porosity and micro (or sub-resolution) porosity. This technique has been successfully applied to a variety of rocks to obtain accurate image-based porosity that agrees well with external helium porosimetry measures [24, 48, 49]. A key aspect of this method is that the macro porous regions are not over-segmented to match external measures when image resolution is limited, as is common when segmenting macro porosity based solely from a dry image of the rock core. Using high-salinity brine, micro porous regions (i.e. clay and partial volume regions below resolution) are highlighted in the pore space, and can be segmented using a global threshold on the differential image.

To segment the fluid phases during the drainage and imbibition fractional flows, a marker based watershed is used [50,51]. Using watershed segmentation, fluid-fluid interfaces can be accurately defined and partial-volume layers (i.e. unphysical water layers) and avoided. The watershed seeds are chosen manually from a 2D histogram of the greyscale and greyscale gradient images; errors associate with this are discussed in section 4.2. The segmented pore-space images can be used to generate continuum scale, macroscopic quantities, such as averaged porosities and saturations. The volumetric averages for porosity and saturation are calculated based on the microscopic image,

$$\overline{\phi} = \frac{\sum_{i,j=0}^{N_v} \delta_{i,j} V_i}{\sum_{i}^{N_v} V_i}, \quad \overline{S}_j = \frac{\sum_{i,j}^{N_v} \delta_{i,j} V_i}{\sum_{i}^{N_v} V_i \overline{\phi}} \tag{1}$$

where $\overline{\phi}$ is the average porosity, $\overline{S}_j$ is the average saturation of phase j, N_v is the total number of voxels in the averaging volume, $\delta_{i,j}$ is the Kronecker delta function and V_i is the volume of each voxel. For the delta function, $j = 0$ is used for voxels with 0 binary value indicating pore space and $j = 1, 2$ for non-wetting and wetting phase voxels respectively.

For the fluid saturations, although an accurate brine phase is needed to calculate interfacial curvatures, the water phase is not used to generate macroscopic water saturations S_w. Since water exists in micro pores below resolution, and therefore cannot accurately be segmented, we calculate the saturation based on the non-wetting saturation S_o and the relationship $S_w = 1 - S_o$. This relies on accurate non-wetting segmentation and knowledge of the total porosity, which is well defined using the differential imaging methodology described above. The non-wetting phase volume fraction estimation is much more robust than the water (wetting) phase, since non-wetting cannot readily enter small pores and throats during the displacement of water. With an estimated maximum capillary pressure in the experiments of $\approx$ 7kPa based on the final non-wetting saturations, the smallest pore radius that a terminal meniscus of non-wetting phase can invade based on young-Laplace law is $r = 2\sigma/P_c = 14.6\mu$m, assuming perfect non-wetting and an interfacial tension σ between fluid phases of 51.16mN/m. This means that with a resolution of 6μm, we will resolve the smallest non-wetting filled pores with at least 5 voxels, giving confidence that we can accurately capture the non-wetting volume fraction in the image.

Following segmentation, the non-wetting phase connectivity is computed from the inlet to the outlet across the entire image using the "Axis connectivity" function in Avizo 9.5. Any voxels with a common vertex are considered connected. Connected and disconnected phases are sensitive to the image resolution and resulting segmentation, with small throats controlling the connectivity across large regions. In a similar argument to the volume fraction calculation, we are able to image the smallest throats during drainage with at least 5 voxels, meaning that we should be able to accurately capture fluid connectivity. Segmentation and subsequent connectivity uncertainty is discussed further in section 4.2.

In order to analyse capillary pressures across scales, the fluid-fluid interface is next extracted. A smooth interface surface was generated using a marching cubes algorithm [25, 46, 50, 52, 53], which was smoothed with a Gaussian filter with kernal size of 5 voxels. This level of smoothing was found as the optimum that produced a smoothly varying curvature estimation with a non-varying mean and variance [25]. A local quadratic curve is then fitted to each point on the triangulated smoothed surface, from which the eigenvalues and eigenvectors represent the principal curvatures and the directions of principal curvatures respectively. The local capillary pressure P_c can be computed through Young-Laplace law:

$$P_c = 2\sigma H \tag{2}$$

where σ is the interfacial tension the fluids, and H is the mean curvature of the two principle curvatures κ_1, κ_2. The distribution of mean curvatures for a suitably sized volume (i.e. above an REV for the system) can then be used to estimate the macroscopic capillary pressure, based on the arithmetic average of the mean curvature distribution [25, 53–56].

When generating curvatures and associated capillary pressures from segmented micro-CT images, there are several potential sources of error that can lead to spurious results; image resolution, segmentation, surface generation/smoothing, connectivity and REV/statistical representativeness. Image resolution is the primary source of error and propagates through all other error sources; in order to capture high capillary pressures, small interfacial features must be resolved and there must be a large enough interfacial area to generate meaningful statistics [56]. Image resolution artefacts are most prominent near three-phase contact lines and arc-menisci created during primary drainage. The interfaces and curvature values near these areas are often omitted or their relative contribution to the final measurement weakened using distance weighting algorithms [53].

The ratio of feature size r to voxel size V_x gives a good indication of the relative accuracy of the resulting curvature estimation $R_f = r/V_x = 2\sigma/P_c V_x$, which can be estimated from the measured capillary pressure P_c and Young-Laplace equation. Previous R_f literature values used in curvature calculations are summarised in Table 1. In these works, when using geological media (i.e. when interfacial areas may be much smaller than in idealised bead packs), the R_f required for accurate curvature estimations is above 5. Most of the previous research considers equilibrium flows, where the fluids have reached stable capillary pressure equilibrium, which improves system stability and accurate interface imaging. Only in [25] are the fluids flowing in a forced regime (at low N_{cp}) throughout the scan; here a relatively large R_f of 11.4 is used to ensure accurate curvature calculations.

In this work, when using an voxel size V_x of 6μm, $R_f = 3.3$ and 6.6 for capillary pressures of 5kPa and 2.5kPa respectively, indicative of typical drainage and imbibition capillary pressures for the oil (Decane) - brine (3.5 wt.%KI) system in Bentheimer sandstones. It is clear that these values are far below that used in previous works when considering forced flow regimes, and result in inaccurate curvature estimates. To alleviate this, we perform high resolution, region of interest scans at 3.5μm and 2μm, bringing R_f during imbibition up to 11.4 and 20 respectively. High resolution

Table 1: Voxel to feature size ratio R_f used in previous literature.

Researchers & year	Sample type	Flow regime	R_f
Lin et al. 2018 [25]	Bentheimer	Forced imbibition	11.4
Li et al. 2018 [53]	Bead pack	Drainage, imbibition at Equilibrium	2.3
Garing et. al 2017 [55]	Bead, Boise, Fontainebleau	Gravity driven Imbibition	7.3 – 27.7
Herring et. al. 2017 [56]	Bentheimer	Drainage, imbibition at Equilibrium	4.5 (min)
Armstrong et. al. 2012 [54]	Bead pack	Drainage, imbibition at Equilibrium	26.4

scans for the final imbibition fractional flow in Bentheimer core 1 are shown in SI Figure 5. The enhancement of the interface representation can clearly be seen by increasing the image resolution and some small scale features that weren't captured in the 6μm image are visible at higher resolutions. The resulting segmentation is also significantly improved for larger features at higher resolutions; the radius of curvature of some interfaces in the 6μm segmentation are clearly larger than those apparent in the raw scan and those generated in higher resolution segmentation. When comparing the 3.5μm and 2μm images, there is a trade-off between enhanced resolution and noise/image artefacts. In the 2μm image, there are clear ring artefacts generated by the duration of the scan and significant zoom, which cause segmentation artefacts. The 2μm image is generally noisier than that at 3.5μm, requiring more significant filtering which reduces the contrast between interfaces making segmentation less accurate. We find here that the 3.5μm image provides the best balance of feature resolution and image quality, with the larger size (significantly above the capillary pressure REV for Bentheimer, see analysis below) generating an improved statistical representation for curvature histograms. To further improve the curvature calculations we use the surface modification technique proposed in [53]. A distance threshold of 1.5 voxels is used to eliminate points close to the contact line, whilst retaining points on small arc menisci features.

3 Theory and modelling methods

In the following sections we describe the theory and modelling (analytical and numerical) methods that are used to analyse and predict continuum scale multiphase flow. This includes model initialisation, parametrisation and solution techniques to compare directly to the experimental observations.

3.1 The continuum framework

In the continuum modelling framework of multiphase flow we use the multiphase extension to Darcy's law, [57]:

$$\boldsymbol{u}_\alpha = \frac{-\boldsymbol{K} k_{r\alpha}(S_\alpha)}{\mu_\alpha} \nabla \psi_\alpha, \qquad \psi_\alpha = P_\alpha - \rho_\alpha g z \tag{3}$$

Here, α refers to the phase (non-wetting or wetting), u_α is the Darcy velocity, $\boldsymbol{K}$ is the absolute permeability tensor, $k_{r\alpha}$ is the relative permeability, μ_α is the viscosity, S_α is the fluid saturation, ψ_α is the phase pressure potential, P_α is the phase pressure, g is the component of gravitational acceleration in the vertical z direction. The conservation of momentum equation (3) is solved along with conservation of mass:

$$\phi \frac{\partial S_\alpha}{\partial t} + \nabla \cdot \boldsymbol{u}_\alpha = Q_\alpha \tag{4}$$

where ϕ is the porosity, t is time and Q_α is an external source or sink of phase α [58]. To close the system of equations we use the relations:

$$S_w + S_n = 1, \qquad P_n - P_w = P_c = P_c(S_w), \qquad k_{r\alpha} = k_{r\alpha}(S_\alpha) \tag{5}$$

where n refers to non-wetting phase, w to the wetting phase, and P_c is the macroscopic capillary pressure.

The macroscopic multiphase extension of Darcy's law (3) can be derived by directly homogeneizing Stokes flow at the pore-scale over a suitably defined representative elementary volume [13, 59, 60] under the following assumptions: inertial and (macroscopic) viscous effects are negligible (including viscous coupling between the phases), the solid

phase is composed of incompressible grains, and the average fluid saturation evolves slowly in space and time through the REV [61]. Similar concepts can be used to derive the macroscopic equation of mass conservation (4), energy conservation if heat transfer is to be considered and solid-phase momentum conservation if considering porous media deformation [13]. The solution of Equations (3) and (4) requires constitutive functional relationships between the relative permeability $k_{r\alpha}$, capillary pressure P_c and saturation S_α, (5), which are usually derived empirically from experiments. These functions are known to exhibit flow rate (i.e. capillary number) dependence [21, 62, 63] and hysteresis (i.e. different functional forms during drainage and subsequent imbibition) [64] due to their non-unique relationship with total saturation (S_α) and the impact of heterogeneities [22].

The drainage relative permeability for the non-wetting k_{rnw} and wetting phase $k_{r,w}$ during drainage are parametrised here using power-law functions:

$$k_{rnw} = k_{rnw}(S_{wirr})(1 - S_w^*)^n, \qquad k_{rw} = (S_w^*)^m \tag{6}$$

where S_w^* is the water saturation normalised to the irreducible S_{wirr}, i.e. $S_w^* = (S_w - S_{wirr})/(1 - S_{wirr})$ and $k_{rnw}(S_{wirr})$ is the non-wetting relative permeability at the irreducible wetting saturation. Power law functions are typically used to describe relative permeability [61, 65], and can be derived at limiting flow regimes directly from pore-scale physics. The macroscopic capillary pressure of the system during drainage is also described using a power-law function, introduced by Brooks & Corey [66]:

$$P_c^d = P_e(S_w^*)^{\frac{-1}{\lambda}} \tag{7}$$

where P_e is the entry pressure, and λ is the pore-size distribution factor.

3.1.1 Representative elementary volume

Essential to this modelling framework is the concept of the representative elementary volume, or REV. An REV is the volume around a material point in space in which the average of a microscopic quantity is independent to further incremental changes in volume [1]. There is generally an upper bound to this volume in heterogeneous media, since there exist macroscopic variations in the continuum property. Similarly, there exists a lower bound when reaching the characteristic length scale of the microscale quantity (i.e. the pore/grain size when considering porosity), at which point the averaging volume becomes meaningless and large fluctuations in the continuum property occur.

There are different REV sizes for different properties, e.g., porosity, fluid saturations [1]. These may also be transient in nature. The REV for porosity and absolute permeability has been studied extensively by [7, 8, 10, 67]. In homogeneous media, this REV appears to have a side length of order ≈ 10 characteristic grain diameters [10, 67], but large variations exist between samples and determination techniques. In contrast, analysis of the REV for multi-phase flow properties, saturation, capillary pressure and relative permeability, has been limited by the difficulty in quantifying these properties at small spatial scales. Fluid ganglia can exist at the scale of individual pores but can also span multiple pores up to the sample length depending on the flow regime (capillary number, viscosity ratio and drainage or imbibition displacement) and pore space morphology, which intrinsically links the ganglia length with the notion of multiphase REV [68].

In this work, we use two approaches to analyse the REV for porosity, saturation, and capillary entry pressure. Firstly, we use a statistical moving average approach to identify an appropriate REV size [10, 69]. We isotropically grow a cubic volume in the centre of the rock core until the volume reaches the core diameter, calculating average property values at each stage. The cube is then moved downstream by one voxel and the process repeated, sampling the pore space in an highly overlapping manner.

A second measure for the REV is determined from the spatial correlation of each property, derived through an empirical semi-variogram. Semi-variograms are often used in geostatistical field-scale modelling to represent the spatial correlation of geological structures [70, 71], but are increasingly used in the analysis of pore [72] and core [40] scale analysis of multiphase flow. The discrete semi-variogram $\xi(r)$ of a quantity ψ can be formulated as [72]:

$$\xi(r) = \frac{\sum_{j=1}^{N_j} \sum_{i=1}^{N_i} l_{ij} \left(\psi_i - \psi_j\right)^2}{2\sigma^2 \sum_{j=1}^{N_j} \sum_{i=1}^{N_i} l_{ij}} \tag{8}$$

where σ is the standard deviation of the property and l_{ij} = 1 if $r - \epsilon < r_{ij} < r + \epsilon$ or 0 otherwise. ϵ is a tolerance used to bin the discrete distances, here set to half the minimum averaging size.

Macroscopic porosities and saturations are calculated directly using the micro-CT images with equation (1) at the associated averaging volumes. Macroscopic capillary entry pressures are then calculated using the capillary equilibrium assumption and the calculated average non-wetting saturations. Here, we first compute the average saturation for the whole core, and find P_c using equation (7). For each smaller averaging volume, we then compute the averaged saturations, and compute a scaling factor for P_c described in 3.1.3, which gives an estimate for the entry pressure of that volume. In this analysis, we use the first fractional flow saturation profile from each experiment, since this exhibits the least end-effects, and gives a good indication of heterogeneity.

3.1.2 Hysteresis

Hysteresis and flow rate dependency in the macroscopic functions (capillary pressure and relative permeability) can stem from several pore-scale mechanisms which are not explicitly incorporated into the classical homogenization approach. Firstly, there is a fundamental difference between pore-scale invasion mechanisms for drainage and imbibition displacements, illustrated by the well known ink-bottle effect [73]; drainage is primarily controlled by the smallest throats in the system whereas imbibition is controlled by the largest pores. Hysteresis can therefore manifest itself as the apparent requirement for a lower capillary pressure during imbibition to achieve the same quasi-static fluid saturation [74]. Secondly, fluid connectivity can significantly impact the flow path and therefore relative conductance of the porous media to a particular fluid phase. During imbibition, snap-off of the non-wetting phase can occur, leading to reduced fluid connectivity and reduced relative permeability compared to drainage [41]. The wetting behaviour of the fluids and porous medium also impacts the fluid connectivity, resulting in different trapping characteristics between water-wet and mixed-wet systems [75]. The contact angle resulting from the wetting state of the porous medium can vary between drainage (θ_A advancing) and imbibition (θ_R receding) with a larger contact angle during drainage ($\theta_A > \theta_R$) resulting in increased capillary pressure.

In recent years, it has been proposed that the capillary pressure function should incorporate the fluid-fluid interfacial area [76–78] or a more detailed description of the geometric state of the fluids [74, 79] to remove this hysteresis, and provide a unique macroscopic description of the capillary pressure through all displacement regimes. While it was shown that including the full geometric state of the fluid-solid phase configurations (described by the four Minkowski functionals - volume, surface area, curvature and connectivity [80]) could fully parametrise the macroscopic capillary pressure [74], providing closure for the increased complexity of these equations at the macroscopic scale is still the focus of ongoing research (see [81, 82] for rigorous derivations of continuum scale multiphase flow equations).

Apparent hysteresis and flow rate rate dependency of macroscopic $k_{r\alpha}$ can also be manifestations of porous media heterogeneity, notably permeability and associated capillary pressure heterogeneity at the REV scale [22, 83–86]. The derivation of the macroscopic flow equations through homogenization relies on the definition of an REV and the fact that fluid saturations vary slowly in an REV; if there is heterogeneity in the porous media structure approaching the size of the homogenizing scale, the derived quantity will be an equivalent property and could be flow rate and/or saturation history dependent [87, 88]. Experimentally, averaged saturations and relative permeabilities are often derived from core-flood experiments, in which the rock core can have heterogeneities approaching the averaging scale. Derived $k_{r\alpha}$ and P_c functions will therefore be impacted by the heterogeneities, and display flow rate dependence even if the intrinsic, homogeneous function does not. This was recently demonstrated in [89] whereby the intrinsic water relative permeability did not exhibit hysteresis, but with the inclusion of structural heterogeneity impacts, the equivalent core-averaged water relative permeability was found to exhibit hysteresis.

It is clear that by rigorous incorporation of the correct pore-scale flow physics and REV level structural heterogeneities, well defined equations and constitutive functions can be obtained that describe continuum scale, macroscopic flow. Whilst it is still unclear as to the exact form that these macroscopic equations should take, in certain limiting cases, i.e. that where the multiphase extension of Darcy's law is valid, we can make use of current macroscopic modelling approaches to directly compare with pore-scale flow experiments, allowing us to asses the validity and limits of current continuum scale models. Rather than removing hysteresis using more independent variables in the governing equations, we parametrise the hysteresis, effectively increasing the complexity of the underlying functions.

The imbibition non-wetting relative permeability is parametrised using the non-wetting phase initial-residual saturation relationship. There have been many empirical models used to describe the evolution of trapping phase connectivity through imbibition displacements, based on the initial-residual non-wetting saturation relationship, see for example [12, 75, 90, 91]. For water wet rocks, the Land model has been found to provide a good match to many experimental datasets [75]. The Land model relationship between the initial non-wetting saturation $S_{nw,i}$ (i.e. the turning point at the end of drainage) and the residual saturation $S_{nw,r}$ (i.e. the end-point of imbibition) is described by:

$$S_{nw,r} = \frac{S_{nw,i}}{1 + C_l S_{nw,i}}, \tag{9}$$

where C_l is the Land trapping parameter. Applying the Land model at different saturation states in the imbibition displacement process yields a relationship for the connected (mobile) non-wetting saturation, as a function of the total non-wetting saturation S_{nw} and trapping characteristics:

$$S_{nw,c} = \frac{1}{2}\left(-\Delta + \sqrt{\Delta^2 - 4\Delta/C_l}\right), \qquad \Delta = S_{nw,r}(S_{nw,i}) - S_{nw} \tag{10}$$

The primary imbibition relative permeability k^i_{rnw} can then be calculated based on the equivalent drainage relative permeability k^d_{rnw} at the connected non-wetting saturation $S_{nw,c}$ [12]:

$$k^i_{rnw}(S_{nw}) = k^d_{rnw}(S_{nw,c}) \tag{11}$$

For intermediate scanning relative permeabilities k^s_{rnw} between the primary drainage and primary imbibition curves, the Killough interpolation method is used [92]. This interpolates the known bounding curves based on the normalised non-wetting saturation S_{norm} between the scanning curve initial (turning point) saturation $S^s_{nw,i}$ and residual non-wetting saturation $S^s_{nw,r}$, which are known from the Land model:

$$k^s_{rnw}(S_{nw}) = k^i_{rnw}(S_{norm})\frac{k^d_{rnw}(S_{nw,i})}{k^d_{rnw}(1-S_{wirr})}, \qquad S_{norm} = \frac{(S_{nw} - S_{nw,r})(1-S_{wirr})}{S^s_{nw,i} - S^s_{nw,r}} \tag{12}$$

In the above formulation, the only parameter needed to fully describe the imbibition non-wetting relative permeability is the land trapping coefficient; this is coupled with the drainage relative permeability to predict imbibition based on the trapping in the system. The interpolation of imbibition scanning curves based on the bounding drainage and imbibition curves has been shown to be comparable to pore network model simulations on similar Bentheimer cores [93].

For wetting relative permeability, there is less dependence on the trapping of the non-wetting phase during imbibition in water-wet media [64], although there have been examples of a slight raising of the wetting relative permeability during imbibition as is seen in the experiments here (see also [20, 94, 95]). This is caused primarily by the wetting fluid occupying larger pores during imbibition than in drainage [61]. This is characterised by using a different exponent in the power-law relative permeability expression (6) for imbibition and using a similar Killough scanning method as per the non-wetting case:

$$k^s_{r,w}(S_w) = k^d_{r,w}(S_w) + \left(k^s_{r,w}(1-S^s_{nw,r}) - k^d_{r,w}(1-S^s_{nw,r})\right)\left(\frac{k^i_{r,w}(1-S_{norm}) - k^d_{r,w}(1-S_{norm})}{k^i_{r,w}(1-S_{nw,r}) - k^d_{r,w}(1-S_{nw,r})}\right) \tag{13}$$

The imbibition capillary pressure P^i_c is formulated in a similar fashion to the drainage case, using a modification of the Brooks-Corey model for drainage, using similar notions as the non-wetting relative permeability during imbibition [96]:

$$P^i_c = P_{ci}\left((1-S^*_{nw,c})^{\frac{-1}{\lambda}} - 1\right) + P_s \tag{14}$$

Here, P_s is the imbibition snap-off pressure, which is near zero for water-wet media. In the original formulation by [96], P_s was omitted, forcing the capillary pressure to zero at the residual. It has been demonstrated experimentally that there may be a finite macroscopic capillary pressure at the end of imbibition in water-wet media [97, 98]. Furthermore, to enable capillary pressure heterogeneity trapping during imbibition, there must be a finite capillary pressure [89, 99], otherwise all points reduce to a capillary pressure of zero and there can be no maintenance of discontinuous saturations as are seen experimentally [100]. P_{ci} can be found by equating the capillary pressures during drainage and imbibition at the turning point:

$$P_{ci} = \left(P_e - P_s {S^*_{w,i}}^{\frac{1}{\lambda}}\right)\left(1 - {S^*_{w,i}}^{\frac{1}{\lambda}}\right)^{-1} \tag{15}$$

Equations (14) and (15) can be used at any point on the drainage-imbibition cycle, both for bounding curves and during secondary scanning loops. Due to the complexity of tracking P_{ci} with subsequent loops, we use an interpolation method to scan between the primary drainage and imbibition curves, again in the manner described by [92]:

$$P^{ds}_c = f_i P^{ib}_c + (1-f_i)P^{db}_c, \qquad P^{is}_c = f_d P^{db}_c + (1-f_d)P^{ib}_c \tag{16}$$

where P_c^{ds}, P_c^{is}, P_c^{db} and P_c^{ib} are the scanning drainage capillary pressure , the scanning imbibition capillary pressure, the bounding drainage capillary pressure and the bounding imbibition capillary pressure respectively. f_i and f_d are interpolating coefficients given by:

$$f_i = \frac{\left(1 + \frac{\epsilon}{S^s_{nw,i} - S^s_{nw,r}}\right)}{\left(1 + \frac{\epsilon}{S_w - (1 - S^s_{nw,i})}\right)}, \qquad f_d = \frac{\left(1 + \frac{\epsilon}{S^s_{nw,i} - S^s_{nw,r}}\right)}{\left(1 + \frac{\epsilon}{(1 - S^s_{nw,r}) - S_w}\right)} \tag{17}$$

where ϵ is a fitting parameter found from experimental results.

Equations (14) - (17) require three parameters to completely describe the imbibition and scanning capillary pressure functions: C_l, P_s and ϵ. C_l is found directly from the initial-residual trapping parametrisation. P_s and ϵ are then found by comparing the predicting imbibition curves to those found experimentally, in our case we compare the curves with estimates of capillary pressure inferred from observations of interfacial fluid curvature (See section 4.3), and we also compare with data published by of [98].

3.1.3 Heterogeneity

The final part of the continuum framework considers the heterogeneity in the system arising from REV level variations in fluid properties, porosity, permeability and capillary pressure characteristics. Fluid properties remain approximately constant throughout the experiment (the pore pressure in the experimental core is 1.5mPa $\pm$15kPa and temperature is 30°C$\pm$ 0.5°C, leading to variations in viscosity and density of decane of $< 0.8\%$ and $< 0.06\%$ respectively; there is similar uncertainty in the brine properties).

Porosity is found directly from the 3D micro-CT image, arithmetically averaged to an appropriate REV. For the permeability, we use the measured core average permeability. While the permeability will vary at the REV scale in the 3D core [85], at the low microscopic and macroscopic capillary numbers in the present experiment, permeability variations at the REV scale have little impact on fluid distributions [22], with core-averaged permeabilities adequate for obtaining equivalent relative permeability estimates. Permeability at the REV scale can be found through pore network modelling [101–103] or through direct simulations [7, 104], although the limited spatial resolution of the CT images in this experiment will necessarily over-predict the permeability [105]. Alternatively, permeability at the REV scale can be inferred through empirical relationships with the REV level porosity and capillary pressure and the known core averaged permeability, i.e. using a Leverett scaling approach [106]. This method has been demonstrated successfully using 3D numerical modelling in several sandstones [85], but requires further constitutive equations to describe the system.

The most prominent continuum property heterogeneity impacting fluid saturations, phase connectivity, and the conductivity of the fluids at low capillary number is heterogeneity in the capillary pressure characteristic [6, 21, 22]. Macroscopic heterogeneities are a consequence of varying pore structure throughout a rock caused by variations in sedimentary deposition and diagentic processes [107]. These heterogeneites exist on a wide range of length scales in sedimentary rocks, occurring as periodic, small scale laminae ($\mathcal{O}$(mm)), as defined bedding planes ($\mathcal{O}$(cm)) [18, 107, 108] as well as larger deformation bands and faults [109].

In order to characterise capillary pressure heterogeneities, we use the imaged fluid saturation heterogeneity as an analogue [110, 111] coupled with the known, intrinsic capillary pressure - saturation function [84]. Observations of fluid saturation during co-injection of fluids at a low fractional flow of the non-wetting phase in the experiments here show large heterogeneities (see Figure 4), and can be used to infer the capillary pressure heterogeneity (See [22, 85, 96]). At steady-state, the macroscopic capillary pressure should be approximately constant throughout the core. This is supported by the saturation profiles in our observations, whereby at $f_{nw} = 0.05$ there are no prominent end effects. Taking an REV scale voxel, we scale the capillary pressure function at a discrete point using the following expression:

$$P_s = \frac{\overline{P}_c(\overline{S}_w)}{\overline{P}_c(S_{wi})} \cdot \overline{P}_e \tag{18}$$

where P_s, $\overline{P}_c(\overline{S}_w)$, $\overline{P}_c(S_{wi})$ and $\overline{P}_e$ are the voxel entry pressure, the intrinsic capillary pressure at the core averaged saturation $\overline{S}_w$, the intrinsic capillary pressure at the voxel saturation S_{wi}, and the intrinsic capillary entry pressure. The intrinsic capillary pressure can be obtained from the model fit (i.e. Brooks-Corey [66]) to experimental porous plate,

centrifuge, or mercury intrusion capillary pressure data. Here, it is constrained by the porous plate data of [98] and our curvature based P_c measurments.

The term $\frac{\overline{P}_c(\overline{S}_w)}{\overline{P}_c(S_{wi})}$ in equation (18) is often referred to as the scaling factor [22]. The above scaling assumes that the capillary pressure function scales only with the entry pressure through the core, and that the function curvature (i.e. λ) and the irreducible water saturation (S_{wirr}) remain the same throughout, an assumption which appears valid for sandstone cores with similar lithologies [40, 84]. Also key to this assumptions, is that the capillary pressure at the REV scale of the voxel is at local equilibrium; this is supported by the low capillary number of the system and the REV analysis in section 4.1. The capillary pressure heterogeneity can also be found using multiple fractional flows [22, 85, 89], however, here we find that the saturation in the first fractional flow gives the best analogue for the capillary pressure, and it is closer to capillary equilibrium than other fractional flows, making the scaling most effective. We choose not to perform any iterative calibration [22], so as to keep the model as simple as possible.

The same scaling factor can be used during both drainage and imbibition, to modify the base capillary pressure functions at a specific voxel [96]. With drainage and imbibition characteristic functions well defined through the Brooks-Corey formulation (see sections 3.1 and 3.1.2 respectively), this scaling factor represents the capillary heterogeneity of the system.

3.2 Numerical modelling

With the continuum framework well posed, we utilise numerical modelling to solve the resulting system of equations, and predict the observed displacement process at the continuum scale in 3D. Equations (3) - (5) are solved numerically on a 3D grid representation of the cores using the fully implicit, isothermal immiscible multiphase porous media flow simulator CMG IMEX^{TM}. The system of equations are discretized into finite-difference form using first order backward differences in time, and central differences in space with upstream mobilities ($k_{r\alpha}/\mu_\alpha$). The orthogonal, Cartesian grid uses block sizes equal to that obtained from the REV analysis, see 4.4.

The model is populated with the intrinsic capillary pressure functions described in sections 3.1 and 3.1.2, with parameters obtained from the experimental observation in section 4.3. REV scale heterogeneity is incorporated through porosity and end-point capillary pressure maps (found through multiplication of the intrinsic capillary entry pressure functions with the derived scaling factors). These are assigned to each voxel of the 3D numerical model, along with core averaged permeability. We prescribe constant fluid properties and temperature throughout the simulations. The intrinsic, rate independent relative permeability function is prescribed across the entire core (see section 4.4) for both drainage and imbibition. The core-averaged trapping parameters (C_l) are used with the Land trapping model to define the connectivity evolution and therefore hysteretic relative permeability and capillary functions for the whole core.

The initial condition is prescribed as a fully saturated medium with $S_w = 1$. To enforce boundary conditions (constant flux at the inlet and a constant pressure at the outlet), we use fictitious inlet and outlet boundary slices. In the physical experimental boundaries, there are two inlet ports which inject the wetting and non-wetting fluids, a pressure transducer tap, and a spiral groove in the end cap designed to spread the fluids evenly onto the inlet face of the core. In the numerical simulation in this work, the fictitious inlet and outlet slices are used to mimic the physical boundary conditions. It should be noted that since we image only part of the core (i.e. the inlet and outlet 5mm are lost due to imaging artefacts), and the model is built directly from the images, the fictitious slices are still within the physical core bounds, and are therefore used to approximate the far field boundary conditions. In the fictitious slices, we use a large permeability ($> 10D$), constant core average porosity, linear relative permeability and a capillary pressure equal to the entry pressure of the system.

To represent the injection of fluids into the system, we use injection wells in the CMG IMEX format. Two wells are used for each fluid component injection which are completed in the central 2x2 voxels in the inlet slice, creating a constant flux inlet boundary condition. Two constant pressure wells are used in the outlet slice to create a constant pressure outflow boundary condition.

One important numerical consideration is the representation of hysteresis in the numerical simulations. Hysteresis is included as per the constitutive modelling described above, but we limit hysteretic effects to the imbibition displacement regimes, i.e. we solve the drainage fractional flows purely with non-hysteretic functions, and start the imbibition co-injection process with hysteretic functions from the end of the primary drainage simulation. In the co-injection drainage fractional flows, the displacement occurs primarily in an invasion-percolation process, although some pore-scale trapping is observed experimentally. When numerically modelling this process at the continuum scale, if hysteretic functions are used, numerical stability and convergence can become problematic due to small-fluctuations in saturation. Furthermore, localised trapping during the drainage co-injection is not observed in the numerical simulations, even with hysteretic functions. This is a fundamental limitation of current continuum modelling approaches; even with hysteresis

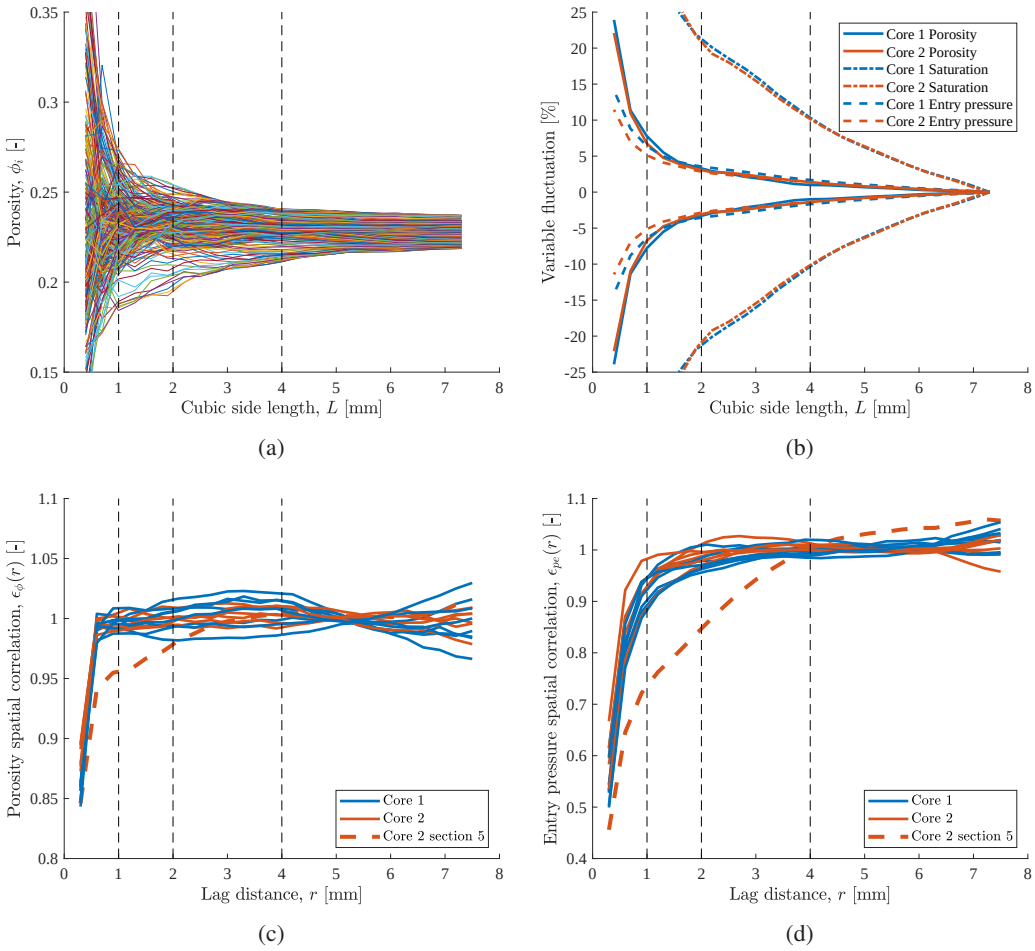

Figure 2: REV analysis for porosity and entry pressure measurements. (a) Core 2 moving average porosity variation. (b) Core 1 and 2 porosity and entry pressure fluctuation with averaging volume. The fluctuation represents the standard deviation of 350 moving average realizations, comparing to that from the largest averaging volume with side length of 7.5mm. (c) Porosity spatial correlation with lag distance. (d) Capillary entry pressure spatial correlation with lag distance.

and heterogeneity in the underlying multiphase functions, we do not observe pore-scale trapping during the primary drainage co-injection process.

4 Results

4.1 Representative elementary volumes

Figure 2 shows the result of the moving average cube calculations and the spatial correlation analysis. The average porosity for each cube realization in core 2 is shown as an example in Figure 2a, highlighting typical porosity variations from the micro to macro scales. The standard deviation of all 350 realizations are displayed in Figure 2b, showing the transition as the volume approaches the largest averaging volume with side length 7.5mm. The standard deviation in fluctuation of both ϕ_i, P_s and S_{nw} are around 10% for an REV with side length of $\approx$ 0.5mm, highlighting the pore-scale inhomogeneity. Above 2mm and 4mm, the fluctuation drops below 5% and 1% respectively for porosity and entry pressure as we approach an REV. The REV for porosity and entry pressure are clearly much smaller than that for saturation, with saturation still showing significant (>10%) variation at averaging volumes of size length 4mm. However, the large saturation fluctuations are not transferred into the capillary entry pressure, which shows much less variation. The capillary pressure is calculated based on capillary equilibrium using the saturation as a scaling; small capillary pressure variations can result in large variations in saturation at low capillary number in steady-state flow.

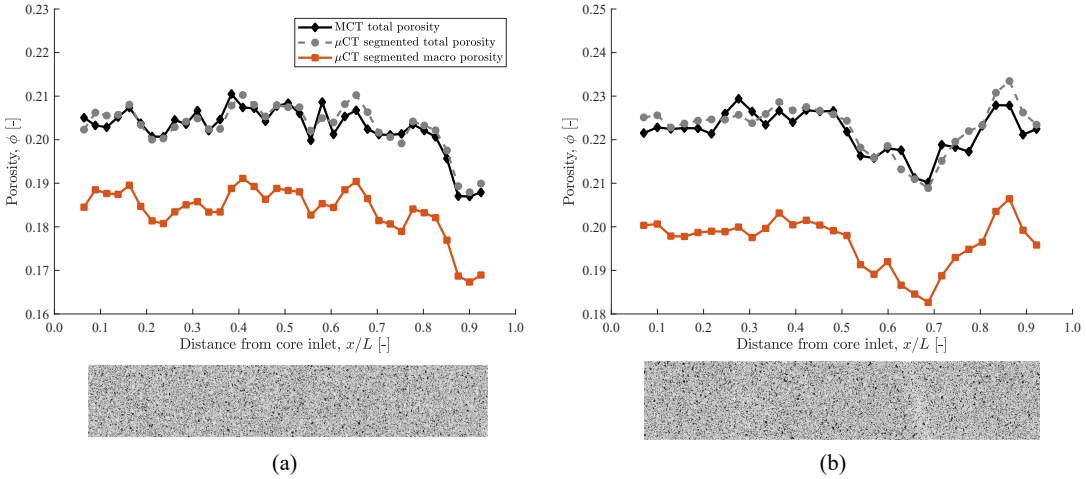

Figure 3: Slice averaged porosities for the two Bentheimer samples calculated using segmented μCT images and differential medical CT images. (a) Core 1, slice width = 1.8mm. (b) Core 2, slice width = 1.9mm. Underneath the porosity graphs is the central slice of the raw, unfiltered dry scan for each core, highlighting heterogeneous regions.

While the porosity and capillary pressure REV are reached within the rock, identified here in the range 2mm - 4mm, the saturation REV could be larger than the sample size.

Previous studies on Bentheimer sandstones have identified an REV for porosity of >1.75mm [29] and saturation of >3.5mm [30], largely in line with the results here. Using similar approaches, [69] identified porosity REVs in the range 0.05 to 8 mm^3 and saturation REVs up to 50 mm^3 in a selection of glass beads and sintered silica samples. [112] calculated porosity REVs >1.4mm in a variety of sandstone and siltstone reservoir samples. Further, in [8], the porosity REV for Fontainbleu sandstone was identified as at least 10mm. The large range of reported REVs for similar sandstone/silica based systems stems from sample variations (i.e. average pore size distributions and permeability), and that from inherent user-bias, i.e. arbitrarily selecting the REV as the point at which the property variation drops below a certain threshold. To remove sample variations, REVs can be described non-dimensionally as $V_{REV} = V/\text{d50}^3$, where d50 is the average grain diameter at which 50% of all grains have a smaller diameter [10]. Using this approach, [10] identified the non-dimensional REV of several sand pack samples as $V_{REV} = 2 \times 10^4$, i.e. a side length d_{REV} of 27 grains. This is similar to that found by [67] in sand-packs ranging from d_{REV} = 5.4 - 15.4. In the samples here, with an average d50 $\approx$ 80μm [26], d_{REV} ranges from 25 - 50 for porosity and capillary entry pressure respectively.

The spatial correlation $\xi(r)$ of the porosity and capillary pressure are shown in Figures 2c and 2d respectively, for 7 distinct cube volumes which cover the length of the sample. Spatial correlation is used for this REV analysis because standard deviation fluctuation of the property with averaging volume leads to an arbitrary REV definition. The lag distance to the sill, or plateau, in $\xi(r)$ indicates the point at which the property variance reaches the variance at the largest averaging volume considered, i.e. an REV is reached. The sill distance is clearly visible at $\approx$0.7mm for porosity and $\approx$2mm for capillary pressure. The plots also highlight the large micro-scale variance by the large 'nugget' or offset in the $\xi(r)$ value at the smallest volume used of 350 μm. $\xi(r)$ computations at volumes smaller than 350 μm result in large computational times, but result in $\xi(r)$ approaching a small nugget near 0. There is also macro-scale, periodic heterogeneity indicated by the periodic variation at large lag distances, indicative of inhomogeneity at large scales. The figure also shows section 5 (out of 7) of core 2, where the tight, low porosity/permeability exists (see Figure 3). Here the sill distance does not occur until at least 4mm, indicating the spatial structure of the low porosity band in the sample.

Using $\xi(r)$ provides an unbiased determination of the REV, at which point the property variance reaches that of the large scale variance. While the moving average REV determination resulted in similar REVs for both porosity and capillary pressure, the spatial correlation distinguishes clear differences in the property structure. In the supporting information, further detailed REV plots are included for porosity, saturation and capillary pressure, along with simulation results presented at various voxel sizes in SI Figures 11-13. Throughout the rest of the article, we use an REV side length of >2mm for voxel computations.

To highlight the macroscopic, REV scale porosity variation through the sample, the imaged-based porosity for both cores is displayed in Figure 3. Alongside this, an external medical CT derived porosity is also shown for validation purposes. The medical CT porosity was obtained using independent differential images of the dry and brine saturated core at a native resolution of 150 μm $\times$ 150 μm $\times$ 500 μm, which is volumetrically averaged to the slice-averaged

values shown in Figure 3. The porosity is calculated through $\phi_{mCT} = (CT_{brine} - CT_{dry})/(CT_{brine,ref} - CT_{air,ref})$, where the references values of brine and air in the core-holder assembly are 991.9HU and -994.4HU respectively. The medical CT total porosity and segmented micro CT porosity agree well with slice averaged L_1 error norms of 0.83% and 1.03% for core 1 and 2 respectively, highlighting the effectiveness of the image normalisation, merging and differential imaging segmentation method. Further details of the method can be found in the supporting information.

The slice average porosities across multiple REVs in Figure 3 highlight the heterogeneity in both cores. In core 1, there is a gradual tailing in the porosity towards the outlet of the sample, seen in both medical and micro-CT porosities. In core 2, there is a defined layer around 2/3rds of the way through the core. This layer is off-perpendicular to the flow direction (Left to right in the image), and represents a significant barrier to flow, discussed later in section 4.2. The variation in total porosity through the samples is maintained almost entirely by the macro porous regions, with the micro porous regions having a near constant porosity through the core.

4.2 Connectivity and hysteresis

Having determined appropriate REVs for the system, we now consider the experimental fluid configurations during the steady-state experiments. Figure 4 shows the connected and disconnected macroscopic saturations for the two Bentheimer cores. The error bars for imbibition fractional flow $f_{nw} = 0.5$ indicate the segmentation uncertainty, generated by varying the greyscale threshold values for the non-wetting phase by $\pm$200 units, i.e. $\pm$3.3% of the original greyscale values. We use this fractional flow since it has significant connected and disconnected non-wetting saturations, allowing uncertainty to be assessed in both phases. The uncertainties in Figure 4 (and presented in tabular form in the SI table 1) highlight the robustness of the segmentation methodology; saturations and connectivity trends are relatively insensitive to the choice of thresholding limits used in the watershed segmentation.

In Figure 4, during drainage at low f_{nw}, the non-wetting phase saturations are highly heterogeneous, showing large fluctuations of $\pm$22.2% and $\pm$ 15.7% around the mean for core 1 and core 2 respectively. The fluctuation is much larger than that apparent in the porosity profiles in Figure 3, indicating the role of macroscopic (above REV) permeability/capillary pressure heterogeneity. As the fractional flow of non-wetting phase increases, the saturation heterogeneity is reduced to $\pm$6.1% and $\pm$ 10.5%, impacted increasingly by the outlet end effect whereby $P_c \to 0$.

During the primary drainage process, there is a small, but apparent volume of disconnected phase, displayed in Figure 4c, d. Low non-wetting phase saturations $S_{nw} \approx 0.1$ can still contain several disconnected ganglia and contribute to variations in fluid conductivity through the sample. In the more homogeneous core 1, the trapping occurs mainly at the core inlet and outlet and is likely due to intermittent connectivity caused by the fluid entering/exiting the core and segmentation connectivity artefacts. The increasing variance in the error bars towards the outlet in core 1 highlights the connectivity uncertainty, which is more prominent at the core boundaries. The sensitivity for other fractional flows is largely similar to that presented for $f_{nw} = 0.5$, and has been tested at several other threshold values. While variations in the connected and disconnected saturation profile are observed, major characteristics (such as jumps in disconnected phase saturation) persist throughout each realization. Note, the total S_{nw} is largely insensitive to changes in threshold values due to the clear gradients between phases which enables robust segmentation.

The disconnected $S_{nw,d}$ phase is much more prominent during drainage in the heterogeneous sample, core 2. This manifests itself around the low porosity/permeability barrier at $x/L \approx 0.7$, where there is a significant jump in disconnected saturation. Localised, high entry pressure regions are known to cause build-ups of S_{nw} during drainage [100], but here we also see an increase in the localised trapping (due to snap-off of non-wetting phase) during drainage. Trapping during a primary drainage process has been recently reported by [113], and could not be described by a classical invasion-percolation process. The mechanism was attributed largely to 'Roof snap-off' during the low capillary number flow regime, which was initially observed by [114] during time resolved, unsteady-state synchrotron experiments. During a Haines jump, some of the wetting fluid in a pore-body can be pushed backwards, towards the throat; if sufficient wetting fluid fills the throat from the corners, it can reconnect and disconnect the non-wetting phase. This process relies on pore space heterogeneity and sufficient aspect ratio between adjacent pore bodies and throats. While this process could be occurring during this experiment, and account for some of the trapping seen during drainage, a more significant mechanism is likely that caused by the pore space heterogeneity itself. At high drainage fractional flows of non-wetting phase, water is displayed downstream and initially trapped ganglia in the upstream section of the core are reconnected. With a reduction in the pore/throats sizes downstream in the low porosity band, the displaced water starts to fill these areas preferentially, and can eventually cause the snap-off of non-wetting phase. A contrast in pore size distributions between adjacent regions necessarily enhances snap off during drainage, due to preferential filling of water in the small pore size region. This mechanism occurs simultaneously with the build-up of connected non-wetting phase behind the low entry pressure region, resulting in a highly heterogeneous saturation profile. This mechanism is likely weaker in the more homogeneous core, since the pore-size distribution is more continuous; displaced water fills the core more homogeneously and Roof snap-off occurs preferentially.

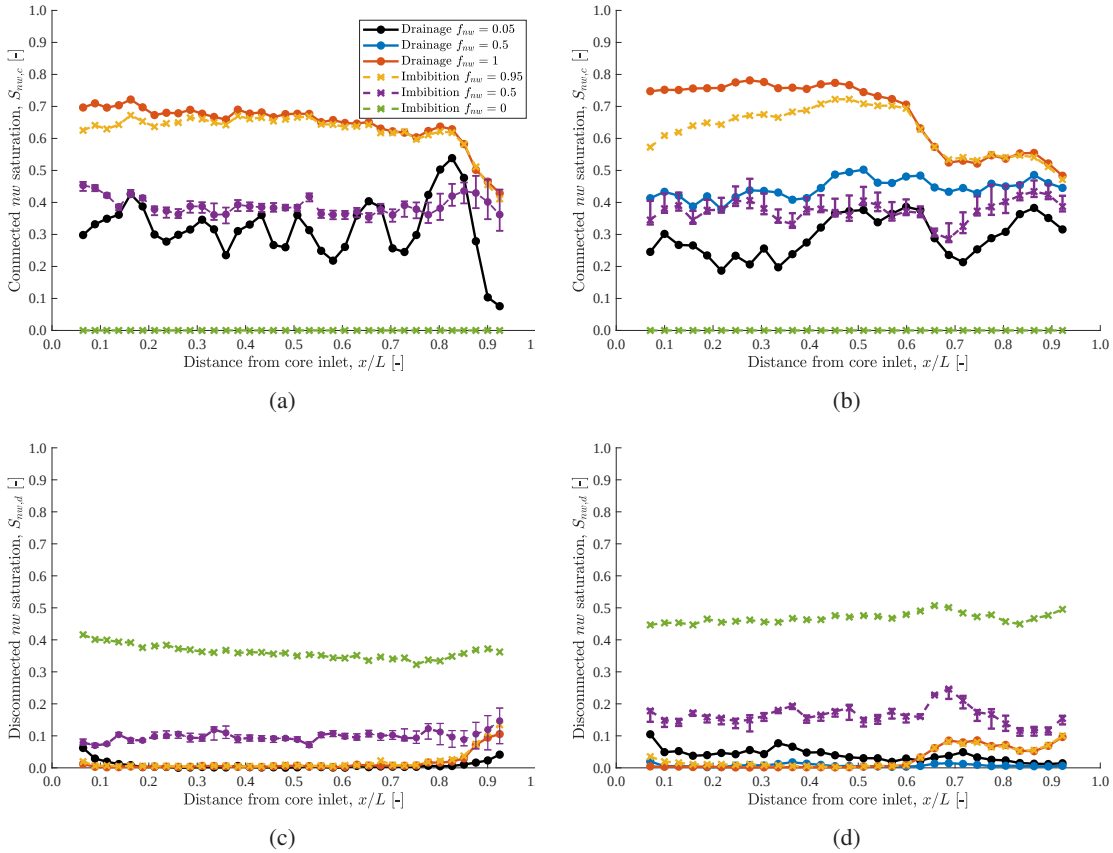

Figure 4: Experimental slice average non-wetting saturations during drainage and imbibition. (a),(c) Connected and disconnected non-wetting saturations for core 1 respectively. (b),(d) Connected and disconnected non-wettin saturations for core 2 respectively. Error bars for imbibition $f_{nw} = 0.5$ represent segmentation sensitivities. Slice thickness's are 1.8mm and 1.9mm for core 1 and 2 respectively.

The pore filling sequence of the connected and disconnected non-wetting phase are shown in Figure 5 for the whole core (detailed pore-filling histograms are shown in SI Figure 10, for 4 sections of the core). During drainage near the percolation threshold, there is a large range of pore sizes invaded by the connected non-wetting phase, highlighting the difference between pore availability and accessibility [115, 116]. The initial invasion percolation process is dominated by piston like displacement and Haines jump pore filling mechanisms [115, 117, 118], followed by slower corner-flow drainage at low water saturations [119]. Based on macroscopic capillary pressures it would be expected that the largest pores in the system would be invaded by the non-wetting phase first, however in Figure 5a, b there remains a significant proportion of the largest pores unfilled at low fractional flows. The pore space topology renders some of these large pores inaccessible; they are surrounded by regions of high-entry pressure. Increasing the capillary pressure as f_{nw} is raised increases their accessibility, and at $f_{nw} = 1$ almost all the largest pores in the system are filled with connected non-wetting phase.

The disconnected non-wetting phase first emerges in the smallest pores in the system, highlighted in Figures 5c, d. Water preferentially swells from the corners of the throats in these regions and eventually re-connects to cause non-wetting phase snap-off in I1 and I2 events [115]; this is true during both primary drainage and imbibition processes. At the end of imbibition, $f_{nw} = 0$, the non-wetting phase is completely disconnected, occupying only the largest pores in the system. The saturations during imbibition are much more homogeneous than those during drainage for the same fractional flow ($f_{nw} = 0.5$) and similar average saturations ($S_{nw} \approx 0.35 - 0.45$) shown in Figure 4. The favourable free-energy change when displacing the non-wetting phase means there is less energy required for the same volume change during imbibition [33, 73]. The capillary pressure required during imbibition to create similar volumetric fluid configurations is lower than that during drainage; this also reduces the overall magnitude of capillary pressure gradients in the rock. With a reduction in capillary pressure gradients, the saturation gradients also reduce, creating a more homogeneous profile through the core.

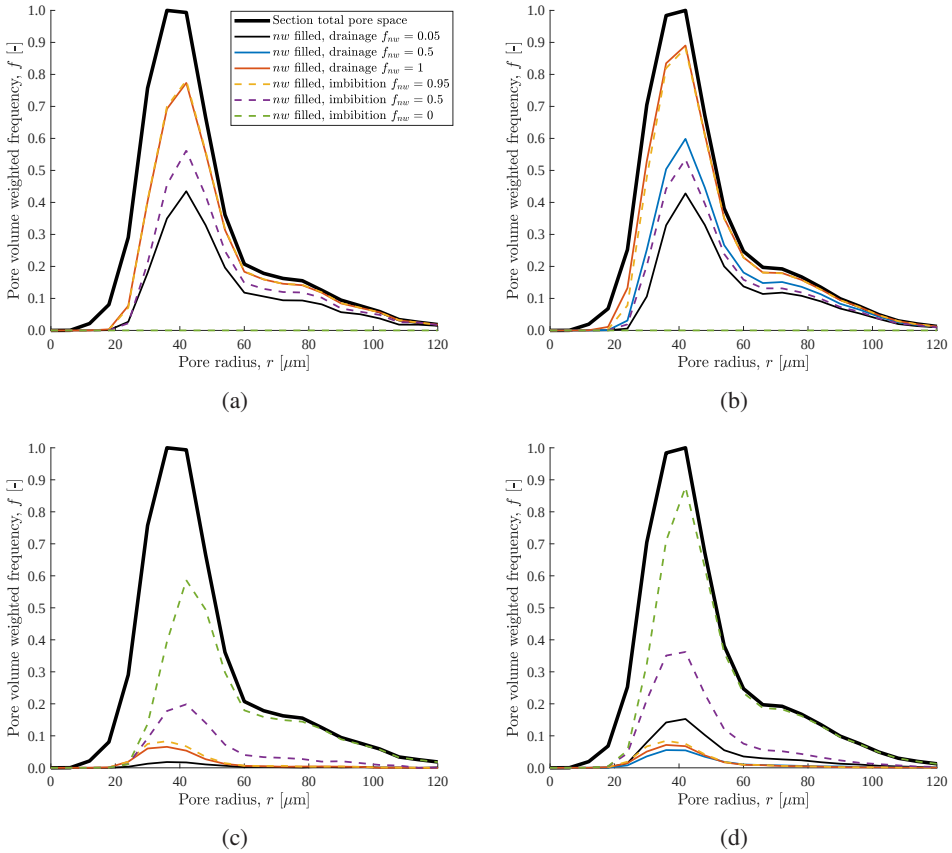

Figure 5: Pore volume weighted histograms showing the non-wetting pore filling sequence during drainage and imbibition, for connected and disconnected non-wetting phases. (a), (c) Connected and disconnected non-wetting filling for core 1 respectively. (b), (d) Connected and disconnected non-wetting filling for core 2 respectively.

The trapping characteristics of the two cores are displayed in the initial - residual plot in Figure 6a, b. The initial saturations here are the connected non-wetting phase at the end of drainage, whilst the residuals are the disconnected non-wetting phase at the end of imbibition minus any disconnected non-wetting phase at the end of drainage. This is key to accurately track the connected phase evolution, and not overestimate the level of trapping by considering already trapped ganglia from earlier in the displacement process. Since we have access to the full connected/disconnected phase steady-state evolution, we can reliably track the initial and residual saturations. Core 1 exhibits typical trapping behaviour of a water-wet sample, with initial saturations $S_{nw,i} \approx 70\%$ which are reduced to $S_{nw,r} \approx 35\%$. The color gradients highlight the distance from the inlet of the core. A typical Land model parametrisation fit is shown for the data, described by equation (9) in section 3.

A proportion of the spread in the voxel data is typically explained with the random error in the saturation measurement from X-Ray CT scanning [22, 84, 120]. Recently in [120] over a wide range sandstone samples this was as high as 7.9-9.8 % for 10mm^3 voxels, which was reduced to 0.22-0.3% for slice averages using a differential imaging medical CT scanner setup. In the micro-CT experiment here, the segmentation sensitivity is linearly propagated through the volume averaging, meaning that large voxels have the same intrinsic uncertainty in saturation as small voxels due to segmentation uncertainty. At $f_{nw} = 1$ during drainage and $f_{nw} = 0$ during imbibition, the non-wetting phase is almost completely connected and completely disconnected respectively, meaning saturation uncertainty is in the range 1.3% - 4.1% (see SI Table 1), essentially smaller than the scatter observed in the plot. Instead, the scatter stems from the inherent REV of the saturation, which is above the voxel size in the figures. The slice averages are taken above the REV and capture the snap-off trapping, which is parametrised well in this case by a Land model [12] for a relatively homogeneous water-wet sample.

In the more heterogeneous core 2 in Figure 6, we see evidence of capillary heterogeneity trapping, i.e. enhanced trapping above that predicted by snap-off processes in a homogeneous core [100]. The general amount of trapping in core 2 has been increased over core 1, even though they exhibit very similar pore-size distributions through the majority

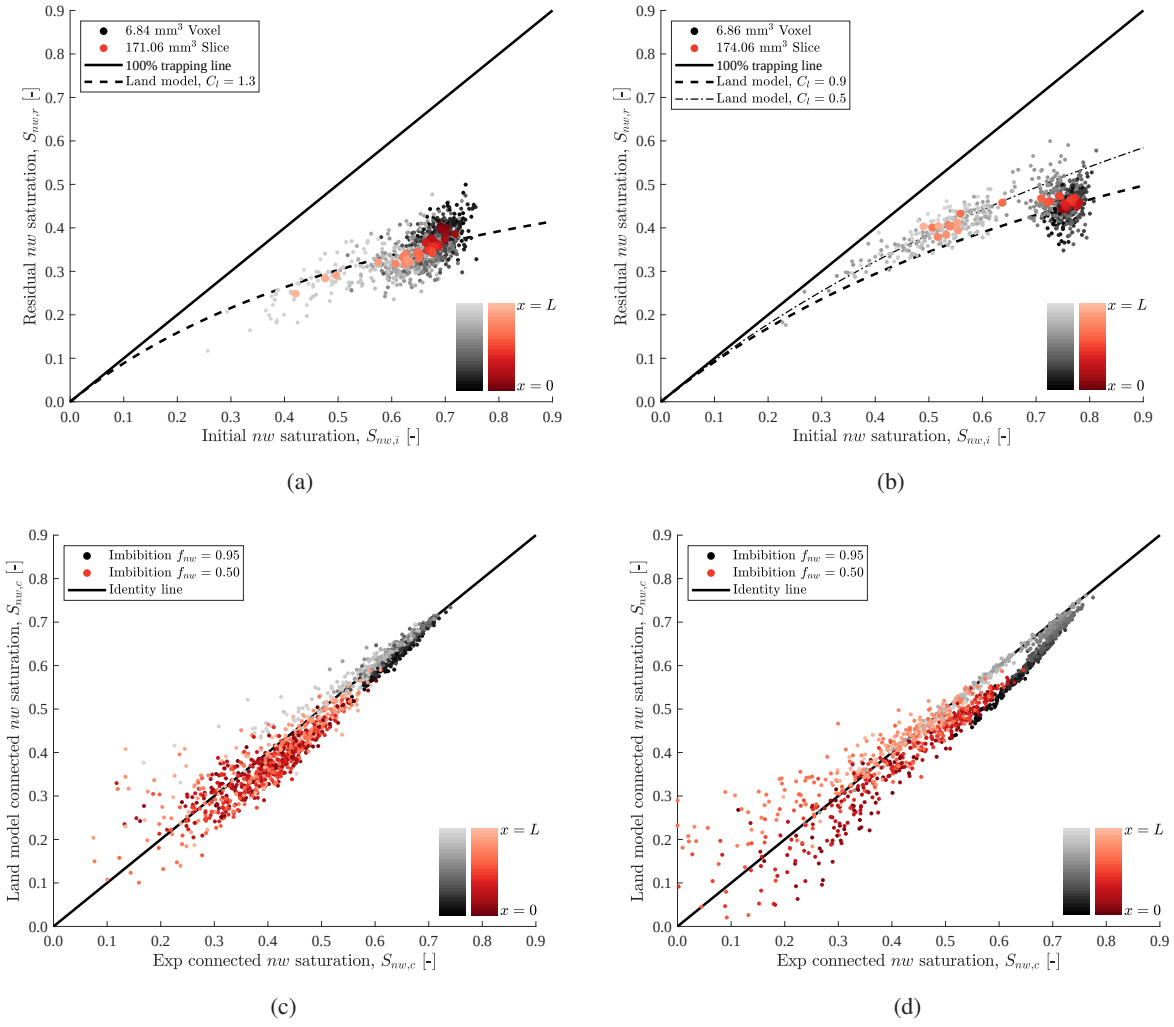

Figure 6: Experimental trapping characteristics at different resolutions. (a), (b) Initial-residual plots for core 1 and 2 respectively, showing trapping measurements at different resolutions with Land parametrisations [12]. (c), (d) Trapping model predictions at different fractional flows compared to the experimental measurements.

of the core (see Figure 5). The low porosity band in core 2 has raised the initial non-wetting saturation compared to core 1, through build-up of non-wetting phase behind low entry pressure regions, and has also trapped it at higher non-wetting saturations following imbibition.

In Figure 6b, the slice average saturations show a similar trend to that at the voxel level, with an increase in the amount of trapping towards the low porosity section (the mid-red/grey color indicates the location of the points near the low porosity region). In the consolidated sandstone in this experiment, the enhanced residual non-wetting profile is due to the heterogeneity of the system and the low flow rate. There are essentially two distinct regions; in the downstream low porosity region, water preferentially imbibes the small pores/throats, snapping off the non-wetting phase at higher saturations than in upstream regions. These are parametrised by different trapping characteristics, shown in Figure 6b. This behaviour does not occur in core 1, even though we see the porosity decrease towards the end of the core; the variation is much more gradual, resulting in less contrast between pore sizes and hence less preferential snap-off occurs.

This kind of enhanced trapping has been observed in larger scale experiments in heterogeneous media [21, 100, 121], but here the results are much more explict. Previous experiments rely on bulk, total saturations to calculate the initial-residual relationships, assuming that all the non-wetting phase at the end of drainage is connected, and it is completely disconnected at the end of imbibition. We have shown that for heterogeneous media this is not always true, trapping can play a significant role during drainage, altering the ‘initial‘ saturation. Indeed, using the initial-residual approach based

on total saturations for the experiments here would over-predict the level of trapping in the core significantly, since some fluid is already trapping at the end of drainage

Further from the initial-residual analysis, the connected saturations can be tracked throughout the imbibition process at different fractional flows. Using equation (10), we can calculate the connected non-wetting phase saturation at any stage of imbibition based on the parametrisation of the initial - residual saturations. Here we use the Land model parameterisation, but this can be any paramterisation of the initial-residual data, e.g. [75,90]. We compare the predictions from the Land model to the directly imaged fluid saturations in Figure 6c and d. In core 1, the connected saturation evolution is well predicted by the Land model for both the $f_{nw} = 0.95$ and 0.5 flows, showing little scatter around the identity line. The inherent assumptions in the connected phase evolution are met in the water-wet homogeneous core, whereby with sufficient initial-residual data the entire mobile evolution can be predicted using the same functional form applied at different 'initial' states.

In core 2, Figure 6d, the model is parametrised with the lower Land coefficient $C_l = 0.9$. At the first imbibition fractional flow $f_{nw} = 0.95$, many of the voxels in the low porosity region are completely disconnected, so the mobile saturation prediction is very good, however for upstream points the model under-predicts the connected saturation. Based on the total saturation, the disconnected saturation predicted from the Land trapping model is roughly 5-10% higher than in seen in the experiments, Figure 4d. The REV scale, high entry pressure region downstream causes a build-up of non-wetting phase in the upstream region, whilst also increasing the phase connectivity; a mechanism called local heterogeneity trapping. This is highly prominent at the low water fractional flow where the capillary pressure is high. In subsequent imbibition fractional flows the connected saturation is again well predicted by the model as the capillary pressure drops, saturations become more homogeneous and snap-off trapping dominates, with the larger spread in points for core 2 indicative of the more heterogeneous core.

Analysing the connected saturation at REV scales gives insight into the fundamental mechanisms for fluid displacement and trapping. Using the simple trapping parametrisation above, the evolution of the connected phase can be predicted and the relative competition of pore-scale displacement mechanisms considered. It is clear that heterogeneity manifesting from the spatial variation in pore-size distribution within a core can completely alter the level of trapping, and the imbibition displacement mechanisms that occur. The temporal evolution of trapping can follow different mechanisms, which are not generally accounted for in macroscopic, continuum scale modelling.

4.3 Capillary pressure from interfacial curvatures

We now compare the macroscopic capillary pressures during imbibition measured through interfacial curvature estimation (as described in section 2.2) with similar curvature measurements in a Bentheimer mm-scale core [25] and porous plate measurements in a macroscopic Bentheimer core from [98]. The results for the subvolumes in core 1 and 2 are shown in Figure 7 against these external measures. The orange solid curve shows the Brooks-Corey model for the drainage data, with P_e = 3.7kPa, λ = 2.7 and S_{wirr} = 0.08. The orange and blue dashed lines show the prediction from equations (14) - (17) with a P_s = 1.165kPa, $C_l = 1.75$ and ϵ = 0.01, derived from the experimental initial-residual curves and imbibition P_c curves of [98]. The imbibition curves show good agreement with the experimental data, capturing both the curvature and endpoint. We note that the scanning curves are also well predicted based on the bounding curves using simple interpolation methods. We note the cores have similar porosities and permeabilities, along with similar pore-size distributions (See [46] for the pore-size distribution, comparing to that given here in Figure 5). We have scaled the independent capillary pressure measurements solely with the interfacial tensions to match our experiment. We choose not to scale with contact angle, since in a strongly water-wet system, the grain roughness renders the effective contact angle near zero for a large range of intrinsic contact angles (i.e. $0^\circ < \theta < 60^\circ$ [122]) making its justification in scaling questionable in anything but a capillary tube [123]. One final point to note is that the drainage MICP data from a sister Bentheimer sample agrees well with the drainage data of [98] (see [25]), but is not shown here for clarity.

The computed capillary pressures in Figure 7 agree well with the exernal measures, showing excellent agreement with the primary imbibition curves of [98] and the mm-scale core computated values of [25]. We see different amounts of snap-off trapping in our system, which alters the residual saturations, but the trend in capillary pressures is remarkably close. Using the region-of-interest, high resolution scanning, we can effectively measure capillary pressures to constrain and provide confidence in our continuum scale modelling. Here, hysteresis in capillary pressure is well parametrised using a model for the disconnected non-wetting phase evolution and the finite, snap-off capillary pressure, as shown in Figure 7. For subsequent numerical modelling, we use the parameters described above, with the trapping parameters $C_l = 1.3$ and 0.9 for cores 1 and 2 respectively to take into account the observed trapping in our experiments.

The error in our capillary pressure measurements can be estimated by considering the error generated through discretisation and segmentation of an idealised surface [25]. In [25], the discretisation error using the surface modification

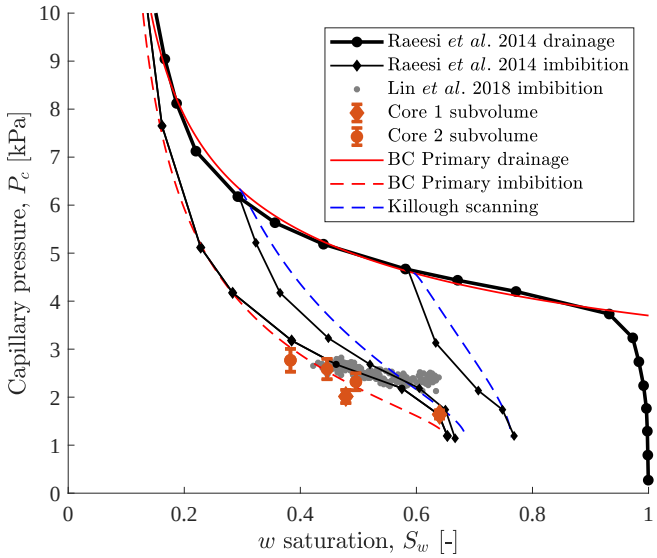

Figure 7: Curvature based capillary pressure measurements for two sub volumes in core 1 and core 2, compared to previous literature measurements on similar Bentheimer cores at the pore and continuum scales.

method mentioned above was roughly 9% using a non-dimensional voxel size of 10 pixels for each feature, and reduced approximately linearly with increasing numbers of voxels. We estimate the error due to discretisation in our system to range between 5.06% and 8.48% for the lowest and highest capillary pressures measured respectively, shown graphically in Figure 7.

In the curvature computation here we use both disconnected and connected non-wetting phases, which have been shown to exhibit similar curvature distributions in water-wet media [25]. While discrepancies exist between connected and disconnected phases (since disconnected ganglia retain the local capillary pressure that they had when they were initially disconnected), over suitably large volumes the overall mean capillary pressure is relatively unaffected by the inclusion of disconnected phases [25]. The final imbibition points here contain only disconnected non-wetting and are likely to be slightly above the true residual capillary pressure value. In mixed-wet media, connected and disconnected non-wetting ganglia can have significantly different capillary pressure characteristics, and inclusion of both phases in macropscopic estimations can lead to signicantly over-predicted capillary pressure [46].

4.4 Numerical modelling and heterogeneity

Further to the experimental (and analytical model) results, we now look to numerically model the observed displacement process at the continuum scale in 3D, using the model parametrisation discussed previously. The numerical models are populated as per the details in section 3.2, and we directly compare the simulated saturations (connected, disconnected) and upscaled relative permeabilities to those measured experimentally. Due to heterogeneity in the model domain, the simulation of the would-be observed relative permeability differs from the input, intrinsic relative permeability and its hysteresis. With the numerical model, we evaluate if we can capture these impacts by comparison with the observed corefloods in which these impacts were present.

Tabulated experimental and simulated data, along with associated uncertainties are displayed in the Appendix, and will be used throughout the discussion herein. Throughout, we compare continuum features centred on upscaled voxels and slices, with sizes based on the REV analysis, the base image dimensions and the allowable scaling to retain an integer number of upscaled voxels. Voxel sizes are $1.95 \times 1.95 \times 1.8$mm and $1.9 \times 1.9 \times 1.9$mm, and slice thickness's are 1.8mm and 1.9mm for core 1 and 2 respectively.

Experimental and simulated relative permeabilities are shown in Figure 8. In each of the plots, the intrinsic, rate independent relative permeabilities used as inputs in the modelling are shown as solid (wetting) and dashed (non-wetting) lines, with black indicating drainage and orange/blue indicating imbibition with different trapping parameters.

The intrinsic drainage curves for both cores are identical, with $k_{rnw}(S_{wirr}) = 0.8$. The non-wetting phase exponent $n = 4.6$ here, which is close to the theoretical scaling for an invasion percolation displacement in 3D [125, 126], i.e.

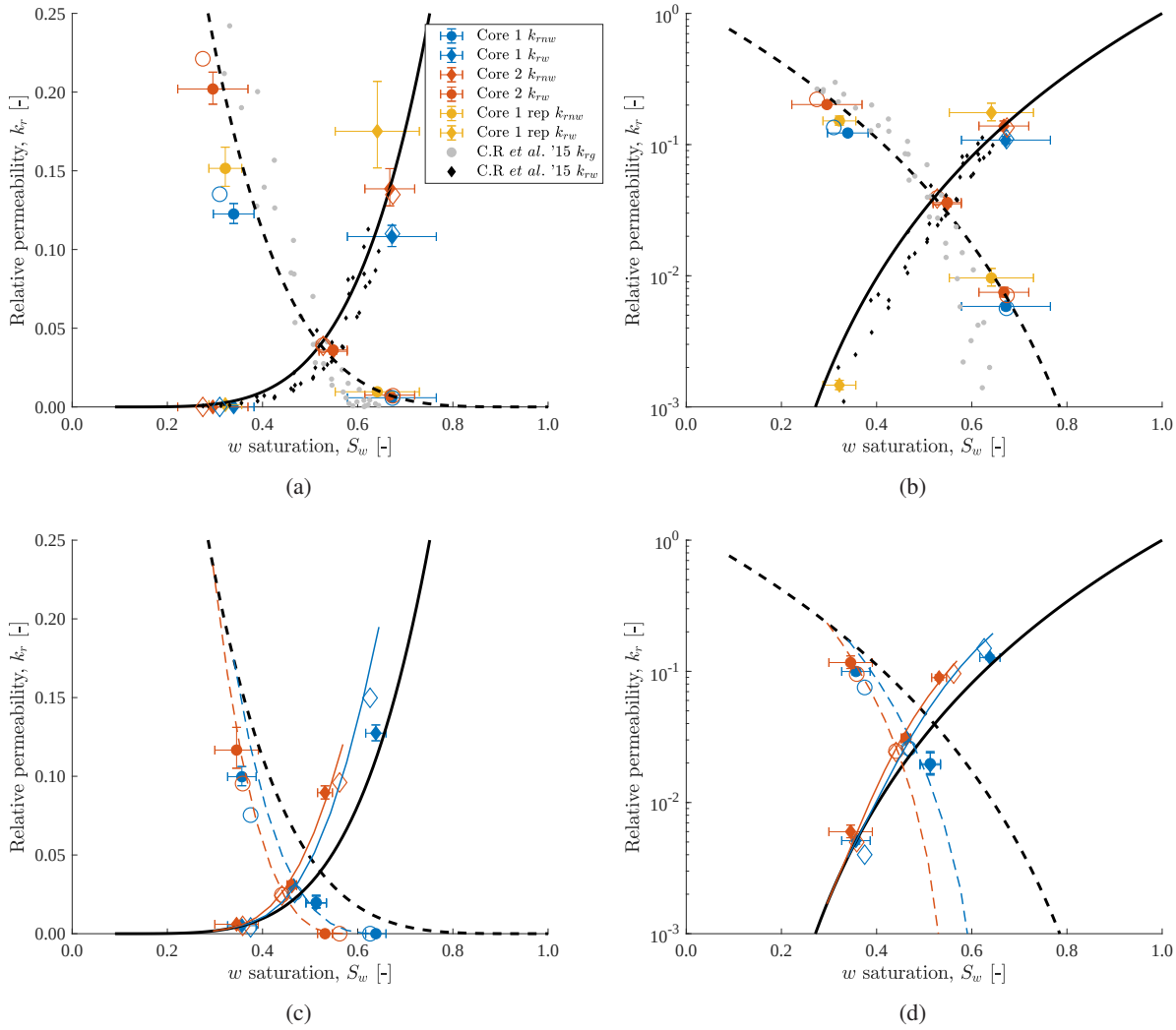

Figure 8: Experimental and simulated relative permeabilities. Closed symbols are experimental data, open symbols are simulations. (a), (b) Drainage relative permeabilities with a linear and logarithmic scale respectively. (c), (d) Imbibition relative permeabilities with a linear and logarithmic scale respectively. Solid and dashed lines are the intrinsic wetting and non-wetting relative permeabiltity functions, respectively. Black lines are for drainage, blue and orange lines are for imbibition with land $C_l = 1.3$ and $C_l = 0.95$ respectively. C.R. *et. al.* 2015 data from [124].

$k_{rnw} \sim S_{nw}^{4.8}$. Indeed, the low fractional flows of non-wetting phase during drainage exhibit invasion percolation displacement, controlled by the pore-size distribution and the availability of pores/throats, see section 4.2. The wetting phase exponent is similar to the non-wetting phase at $m = 4.4$; we note that during thin-film flow the exponent can be expected to scale as $k_{r,w} \sim S_w^4$ [61], which is observed here at low wetting phase saturations. For imbibition, the non-wetting relative permeabilities are the same as those during drainage at the corresponding connected phase, which is modelled through the Land trapping parametrisation as described in section 3.1.2. Here, C_l = 1.3 and 0.9 for the two cores respectively (see Figure 6). The wetting phase relative permeabilities during imbibition are modelled with the power law function in equation (6), with $m = 3$.

The relative permeability experimental error bars arise from the standard deviation in experimental pressure differential, which is most prominent at low wetting saturations due to the low pressure differential. Saturation error bars represent the standard deviation in slice average saturation from the whole core average, highlighting heterogeneity at low f_{nw} and end effects at high f_{nw}. These uncertainties are generally larger than those arising from segmentation, see Figure 4. In Figure 8 we also display the repeat drainage experimental data in yellow, highlighting the consistency in relative permeability between measurements.

During drainage, the crossover point $S_w > 0.5$ indicates a water-wet core. The core averaged relative permeabilities are well captured by the numerical model, with relative errors $< 11\%$. Core averaged saturations errors are also very low $< 5\%$. The deviations of both the experiments and simulated data points from the input curve reflect the impacts of rock heterogeneity. The proximity of the simulation points to the experimental points is a measure of the ability of the parameterised model to predict these impacts. The same intrinsic relative permeability is used for both cores, but the distinct spatial heterogeneities manifest in different equivalent relative permeabilities at the largest (core) averaging scale.

The magnitude of the capillary pressure heterogeneities are relatively low in the samples, with $\eta = \sigma(P_e)/\mu(P_e) = 0.095$ and 0.080 for cores 1 and 2 respectively, similar to that reported for Berea cores $\eta \approx 0.1$ [96]. For stronger heterogeneities, such as that seen in reservoir cores (e.g. a Bunter core with $\eta \approx 0.17$ [21, 22]), or carbonate samples (e.g. Indiana limestone $\eta = 0.21$ [127]) the relative permeability variation can be much lager, with orders of magnitude variation between different capillary number experiments [21]. The drainage data and intrinsic relative permeabilities are also consistent with the viscous limit cases from [124], also shown in the plots. The intrinsic, or viscous limit relative permeability described here is that effectively obtained from a homogeneous fluid distribution without capillary pressure heterogeneity effects, during connected pathway flow. It is not to be confused with a relative permeability derived at a high pore-scale capillary number, which may have macroscopic viscous and inertial impacts [63] as well as significant amounts of pore-scale fluid intermittency [42].

Core length profiles and voxel by voxel comparisons of the simulated and experimental drainage saturations are shown in Figure 9. In core 1, the heterogeneous, near periodic saturation profile is well captured at both low and high non-wetting fractional flows. Using the low fractional flow saturation to scale the capillary entry pressure in the core has resulting in a strong prediction across the fractional flow regime. Without this scaling, even with strong permeability contrasts the saturation profile would be homogeneous. For core 2, the saturation heterogeneity is somewhat under-predicted, with significantly more scatter from the identity line on a voxel by voxel basis. In this experiment, the higher differential pressure renders the displacement closer to the viscous limit, and hence scaling the entry pressure with the non-wetting saturation is less effective. This is apparent also in the proximity of the equivalent relative permeabilities to the intrinsic curves in Figure 8. We note that by increasing the variance in the entry pressure field in an iterative manner [22, 85, 127], the saturation in the core can be well predicted, but the model potentially becomes less predictive for other flow regimes to those used in the inversion process. Using multiple fractioanl flows and flow rates in the inversion can improve the predictive nature of the model [22].

In the experiments, we also observe a significant proportion of disconnected non-wetting phase during drainage, which is not predicted by the model, even with hysteretic relative permeability and capillary pressure functions. The displacement occurs in a macroscopic invasion-percolation process in order of entry pressure [128], with all voxels increasing monotonically in non-wetting saturation once invaded. It is possible that the disconnected non-wetting phase aids the localised saturation build-up of the connected phase, increasing the saturation heterogeneity in the system, something that should be considered in future model developments.

The simulated imbibition relative permeabilities are compared to the experimental data in Figure 8c, d. The experimental data is generally less well predicted than drainage, with average saturation errors $\approx$10% and relative permeabilty errors $\approx$20%, although they are as high 30% in some case, see Tables 4 and 5 below. The largest error is in the middle fractional flow $f_{nw} = 0.5$ during the core 1 experiment, where the experimental relative permeability and non-wetting saturation are significantly lower than the model. The experimental pressure differential during this fractional flow is highly oscillatory with a standard deviation of 23.5% about the mean (see the pressure signal in SI Figure 7). This is frequently observed and could indicate increased flow dynamics at the pore-scale [45] which could impact the saturation

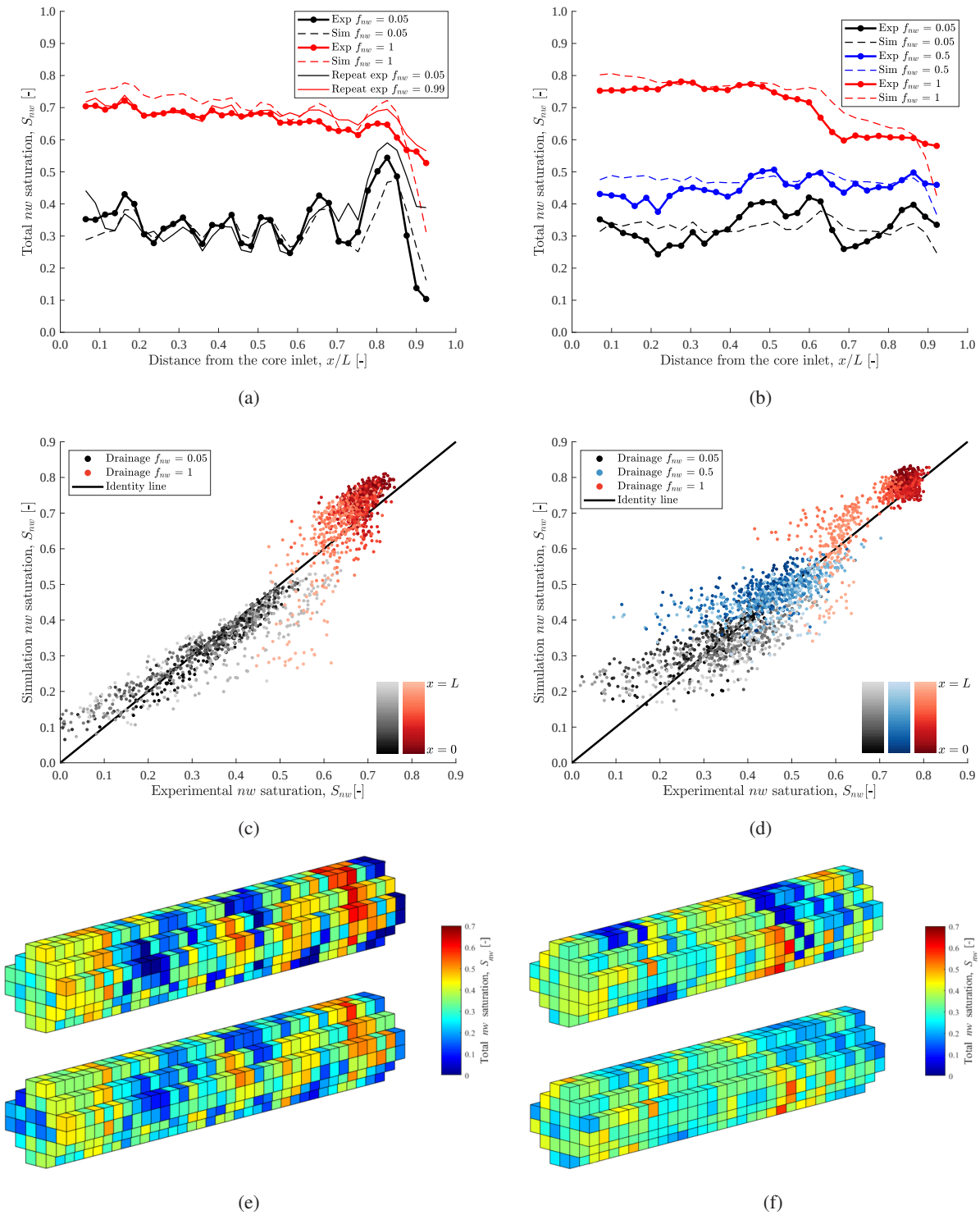

Figure 9: Drainage simulation results compared to experimental data. Left hand side - core 1, right hand side - core 2. (a), (b) Slice average total non-wetting saturation across the core. (c), (d) Voxel level non-wetting saturations. (e), (f) 3D non-wetting saturation rendering for $f_{nw} = 0.05$ top - experiments, bottom - simulations. Note the cores are shown horizontally but are orientated vertically in the experiments.

distribution. Despite the relative error in the simulated and experimental results, we note that they are largely in line with experimental uncertainties which are larger during the imbibition fractional flows. The numerical model is able to capture the key characteristics in the relative permeability variation from the intrinsic curves, as well as the variations from drainage with relatively simple functional parametrisation based on the residual trapping. The imbibition relative permeability is therefore more 'predictive' in a sense than drainage, requiring less parametrisation.

As with the drainage relative permeability, we see the impact of capillary pressure heterogeneities in the derivation of equivalent imbibition functions at the core-scale, which differ from the intrinsic functions. The reduced impacts of heterogeneity during imbibiton have rendered the equivalent functions closer to the intrinsic, which are well predicted by the interpolated scanning functions using Killough's method [92]. We note that in the numerical simulation, the drainage displacement does not reach the irreducible water saturation due to the low capillary number, meaning that all subsequent imbibition displacements essentially occur on scanning paths from the primary drainage curve. Using the primary drainage and imbibition curves as inputs, the numerical model with trapping parametrised by the Land model does remarkably well at scanning the imbibition displacement.

The raising of the water relative permeability during imbibition is captured in the model using a decrease in the power law exponent, resulting in a good prediction of the experimental data. In these relatively homogeneous water-wet cores, this variation in relative permeability is slightly unexpected, since it was anticipated that the water displacement would be very similar during drainage and imbibition. A raising of water relative permeability implies a move to displacement in larger pores; a mechanism generally associated with changes in wettability [61]. In the low pressure/temperature decane - brine system here this however, is unlikely. The slight raising in water relative permeability during imbibition has been seen in other experimental data (see [20, 94, 95])), and could also be an impact of the heterogeneity in the system. Hysteresis appears more prominent in core 2, which could be a consequence of the enhanced snap-off trapping in the low porosity region, which causes the water to displace the non-wetting phase in cooperative pore filling events upstream. Filling larger pores here would result in enhanced conductivity through the system compared to the thin-film and corner flow occurring more prominently during drainage. Although water hysteresis is less pronounced in core 1, we note that without hysteretic water relative permeability during imbibition, the simulated pressure differential is much lower across all fractional flows, and does not capture the experimental data well.

The imbibition saturation profiles along with trapping characteristics for the simulation and experimental data are shown finally in Figure 10. In Figures 10a, b we observe the impact of hysteresis in multiphase flow; the saturation heterogeneity in the system has been significantly reduced compared to drainage (see Figure 9a,b above), an impact primarily due to the capillary pressure hysteresis. The spread in voxel level saturation data is also significantly reduced in Figures 10c, d, which is well captured by the model. We note that the numerical model here is performing in a much more predictive manner than during drainage; the function parametrisation relies solely on the drainage data coupled with final trapping data, which is used with physical arguments to construct the imbibition functions. The capillary pressure heterogeneity during imbibition is scaled using the same parametrisation, equation (18), as that during drainage, and is able to reproduce the experimental saturation variation through the core.

The numerical model is also able to reproduce, to some extent, the observed trapping at $f_{nw} = 0$, shown in Figures 10e, f. Here, most of the simulated data points fall exactly on the trapping model used for the simulations, i.e. the trapping occurs primarily through snap-off. However, there are data points with non-wetting saturations higher than that given by the trapping model, indicating enhanced capillary heterogeneity trapping, as seen in the experiments. Physically, in the model this occurs when the voxels surrounding a central voxel lose connectivity and the saturation reaches the residual, but the voxels retain a higher residual capillary pressure (due to the P_e scaling) than the central voxel. The non-wetting relative permeability in the surrounding voxels is by definition zero. The central voxel non-wetting saturation is still essentially 'connected', i.e. it has non-zero relatively permeability at the continuum scale since it is not at the residual, but the saturation cannot reduce further due to the higher capillary pressure in the surrounding voxels. The saturation of the central voxel therefore remains at the same state throughout subsequent imbibition, and is effectively trapped through local heterogeneity. We note that this mechanism is capillary heterogeneity trapping during imbibition, which is often incorrectly discussed in terms of the drainage process, whereby localised accumulations of non-wetting phase build up behind capillary pressure barriers. The process is similar, but here is defined by the connectivity of the system.

Key to modelling this process during imbibition is having a finite, non-zero macroscopic capillary pressure at the residual non-wetting saturation [89, 99], as shown in Figure 7. This finite capillary pressure is observed experimentally [98], but is often reduced to zero, or negative values by further reducing the wetting phase pressure relative to the non-wetting phase. There is generally no further production of non-wetting phase, and the end-point of the capillary pressure curve can be arbitrarily defined. For water-wet media, the end-point is often defined as $P_{cei} = 0$ [96], but this leads to under-estimation of the amount of heterogeneity trapping in the system. If all points in the core can reduce to a capillary pressure of zero at the residual, essentially no gradients are observed in the capillary pressure, which inhibits any local heterogeneity trapping described above. In fact, given enough time, the system will completely reduce to that predicted

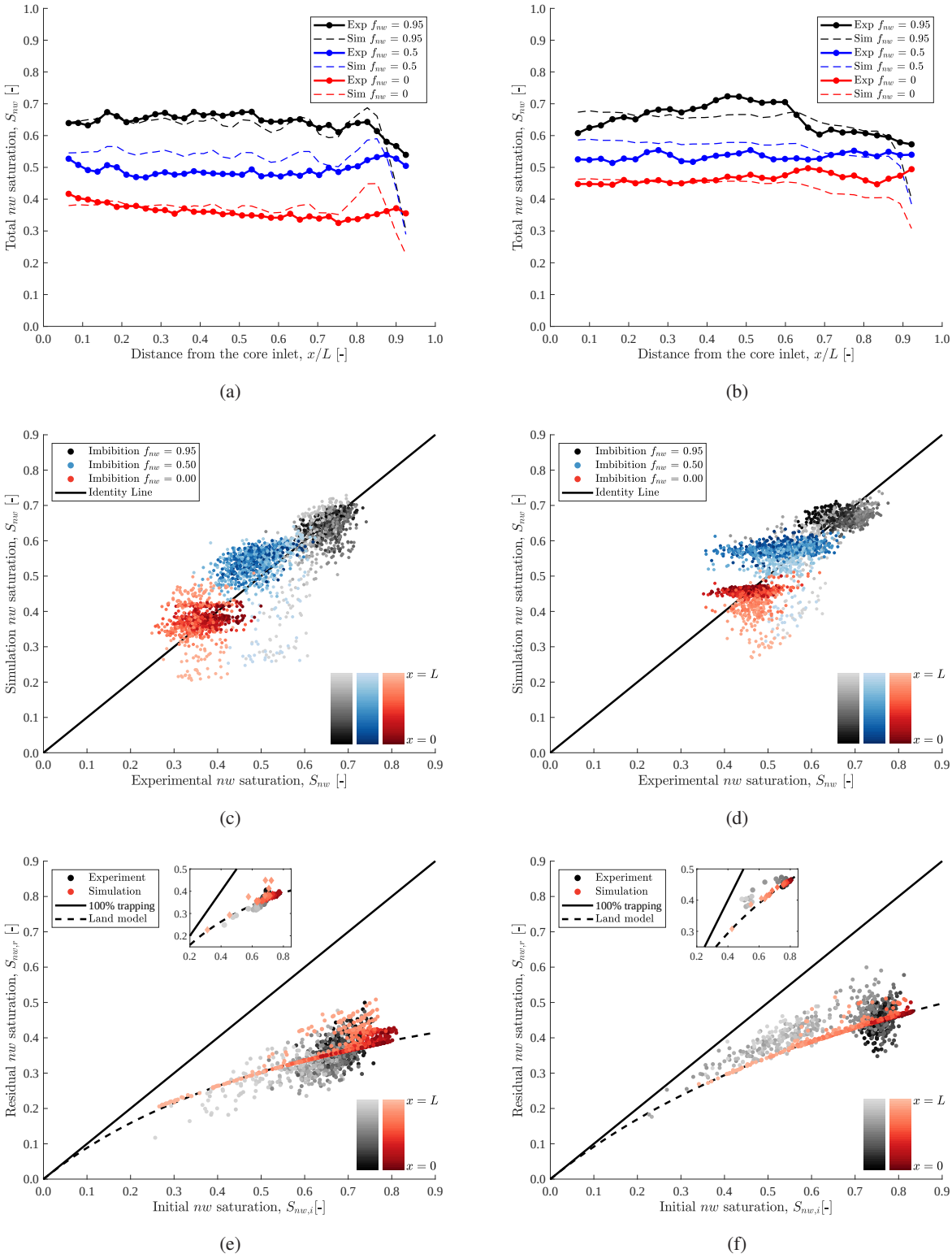

Figure 10: Imbibition simulation results compared to experimental data. (a), (b) Slice average total non-wetting saturation across the core for core 1 and core 2 respectively. (c), (d) Voxel level non-wetting saturations for core 1 and core 2 respectively. (e), (f) Voxel level initial-residual characteristics for for core 1 and core 2 respectively. The zoom in box plots show the slice average trapping results.

by the snap-off trapping model, which is clearly not the case. The finite value of capillary pressure here can also be negative for mixed or oil wet systems, and there can produce local heterogeneity trapping is capillary pressure gradients can be sustained in the system [128].

The voxel and slice average trapping results in Figures 10e,f highlight the REV of the system. At the slice level, there is a reduced impact of heterogeneity trapping, both in the experiments and simulations, but it is still observable, pushing the data off the intrinsic trapping curve. In previous reported trapping results, we see a large spread of data for similar sandstone cores [6], which may be a result of capillary heterogeneity trapping impacting the averaged trapping results. Distinguishing between the trapping mechanisms will allow the intrinsic, snap-off trapping nature of the core to be observed, which is what is ultimately modelled using an initial - residual parametrisation.

In the simulations, we see more capillary heterogeneity trapping in core 1, since the heterogeneity variance is larger in the model compared to core 2. In the experiments, while we see a larger variance in the trapping in core 2, when considering the two distinct regions, the variance of each region is less than core 1. We model the experiment using only a single snap-off trapping parameter, to enable us to distinguish between trapping mechanisms, but for core 2 there may be two distinct snap-off trapping parametrisations for the different regions. From the experiments, it is difficult to distinguish between the two trapping mechanisms, and to pin down whether there is a fundamentally different level of snap-off trapping occurring, or if it is enhanced by capillary heterogeneities, since we only view the disconnected ganglia and cannot tell if they are at the final residual. Using the model we can distinguish between the two mechanisms, which allows the relative importance to be gauged. Recently [120] reported for a range of sandstone systems that the level of heterogeneity trapping can be the same order of magnitude as that due to snap-off, however the results were extrapolated from many different sandstone cores, which would have intrinsic differences in their snap-off trapping capabilities due to the pore/throat-size distributions; this was not considered.

The simulated results here reveal that boundary conditions during imbibiton are important for the model performance, but are difficult to estimate from the experiments. It is clear from the experiments that end effects (i.e. tailing of the non-wetting phase towards the outlet) are reduced, or inverted during imbibition, and proper inclusion of these impacts in models is crucial. Here, we use the imbibition residual capillary pressure, P_{cei}, as a constant capillary pressure for the boundary condition. Since the capillary pressure reduces significantly during imbibition, using a lower boundary condition is needed, otherwise artifical capillary pressure gradients are created in the core (i.e. if one uses the drainage entry pressure P_e). Using this condition, we are able to reduce the impact of end-effects compared to drainage, and correctly capture capillary pressure heterogeneity in the core, but we still somewhat underestimate the saturation at the outlet. It is also important to note that at low differential pressures, the capillary pressure conditions in the core and the boundary are important, since they can be of similar magnitudes. Using a high outlet capillary pressure will raise the whole core capillary pressure in a similar manner to using the drainage capillary pressure during imbibition, generally resulting in a reduced pressure differential and an over-prediction of the relative permeability.

It is key to model hysteresis in capillary pressure to predict the variation in saturation profiles between drainage and imbibition and the impact of trapping [89], but this is often neglected in core-scale modelling [120] and in larger field-scale modelling [129]. In this work, through the combined use of pore-scale imaging and continuum scale modelling we have demonstrated a multi-scale approach to analyse immiscible displacement in porous media.

5 Conclusions and future outlook

In this work, we combine multi-scale X-ray observations of drainage and imbibition displacements with continuum numerical models to assess REV for single and multiphase flow properties, the relationship between hysteresis and non-wetting phase fluid connectivity, and the role of small scale continuum property heterogeneities on the upscaled manifestation of relative permeability. The analysis was performed using a water wet fluid-rock system, decane and water, in a homogeneous and a heterogeneous Bentheimer sandstone rock core.

The REV for both porosity and capillary pressure characteristic curves is approximately 2mm for both heterogeneous and homogeneous samples. In contrast, the REV for saturation exceeds 8mm, the largest scale investigated. This indicates a situation where a minimum REV for multiphase flow properties is smaller than length scale associated with continuum property heterogeneity. Capillary pressure characteristics control heterogeneity in the fluid distribution, and therefore must be accounted for in the interpretation of core-scale observations of relative permeability.

Predictions of fluid connectivity and hysteresis during imbibition using the Land trapping model are validated against the experimental observations for the homogeneous Bentheimer sandstone. Fluid morphology is increasingly viewed as essential for a rigorous representation of upscaled flow properties. In this case of a homogenous rock samples, a simple measure of that morphology, the connectivity, is sufficient to fully parametrise the continuum flow properties across displacement pathways. In contrast, fluid connectivity is higher than anticipated by the Land model for a given location

on the relative permeability hysteresis pathway in the heterogeneous rock. This is due to larger scales of non-wetting phase trapping upstream of capillary barriers. In this case multiple scales of flow phenomena are required to describe the full core-scale flow across drainage and imbibition pathways. Fluid connectivity corresponding to the pore-scale trapping phenomena must be combined with information about continuum scale immobilisation behind local capillary barriers for a full description.

Continuum scale numerical models of the rock cores are largely able to predict the impacts of small scale heterogeneities on the upscaled saturations and relative permeability. Parameterising these models with properties obtained at the 2mm scale identified by the REV analysis allowed for accurate predictions of fluid distribution and upscaled relative permeability. This confirms that the both heterogeneity and hysteresis in the capillary pressure characteristics are key to the upscaled manifestation of relative permeability, even at the cm-scale of the rock cores used in this work. This suggests that for physics-based modelling of subsurface multiphase flow, a workflow is required which successfully accounts for the upscaled impacts of these properties.

The experimental dataset presented in this paper, and available for download online, provides an excellent benchmark for developing and validating continuum scale modelling approaches. Key to future developments of continuum models are the thorough inclusion of connectivity evolution during both drainage and imbibition (i.e. the roof snap-off mechanism that can occur during primary drainage), and the incorporation of these effects with REV scale heterogeneities. Further developments are also needed to incorporate multi-scale REV heterogeneities, such as those occurring in carbonate rocks [127].

Alongside this, continuum models must also incorporate the impacts of high N_{cp} flows, that lead to intermittent fluid connectivity [43, 44] and enhanced ganglion dynamics [45]. While the use of extended Darcy's law with REV scale heterogeneities is largely sufficient for capturing the flow regimes presented in this paper, and is sufficient for many field-scale applications, it is likely that extended models, possibly based on the fundamental thermodynamics of the system may be needed to capture the full manifestation of immiscible pore-scale physics at the continuum scale [58, 82]. It is our hope that this work and dataset will serve as a base to advance such endeavours, leading to predictive, multi-scale continuum models.

6 Acknowledgements

We gratefully acknowledge funding from the Shell Digital Rocks programme at Imperial College London and the Natural Environment Research Council (Grant number: NE/N016173/1). We acknowledge Computer Modelling Group (CMG) for providing access to IMEX. We thank Ab. Coorn from Shell for sample preparation and Steffen Berg for helpful comments. We also thank Martin Blunt, Branko Bijeljic and Ronny Pini for help with the experimental design and insightful discussion. We thank Chris Zahasky for useful comments on the draft paper.

Data associated with this work is currently being uploaded to an on-line data repository (raw X-Ray CT imagery and segmented data, post-processed porosity and saturation Matlab data, CMG simulation files and Matlab processing files). Due to the large data size ($\approx$ 2.5Tb in total for all raw and segmented X-Ray CT data; each full core 6μm image is $\approx$ 80Tb), the full data set is currently hosted on the Imperial College London research data store, and can be downloaded via the free Globus client. Please contact the authors to obtain download permissions.

7 Appendices

Experimental saturations and differential pressures, along with uncertainties are displayed in Tables 2 and 3 for core 1 and core 2 respectively. Simulated saturations and relative permeabilities, along with errors are displayed in Tables 4 and 5 for core 1 and core 2 respectively

Table 2: Tabulated core averaged experimental saturations, differential pressures and relative permeabilities for core 1, along with relative uncertainties.

Fractional flow	S_{nw} [-]	S_{nw} uncert [%]	ΔP [kPa]	ΔP uncert [%]	k_{rnw} [-]	k_{rw} [-]	k_r uncert [%]
Dra f_{nw} = 0.05	0.328	22.16	4.359	6.16	0.0058	0.1082	6.60
Dra f_{nw} = 1	0.661	6.08	4.155	5.13	0.1226	0.0000	5.43
Imb f_{nw} = 0.95	0.643	4.44	4.848	6.06	0.0997	0.0051	6.49
Imb f_{nw} = 0.5	0.487	4.22	12.828	19.03	0.0198	0.0193	23.54
Imb f_{nw} = 0	0.362	5.55	3.900	3.92	0.0000	0.1274	4.10

Table 3: Tabulated core averaged experimental saturations, differential pressures and relative permeabilities for core 2, along with relative uncertainties.

Fractional flow	S_{nw} [-]	S_{nw} uncert [%]	ΔP [kPa]	ΔP uncert [%]	k_{rnw} [-]	k_{rw} [-]	k_r uncert [%]
Dra f_{nw} = 0.05	0.333	15.73	7.197	8.47	0.0075	0.1386	9.25
Dra f_{nw} = 0.5	0.452	6.53	14.857	5.12	0.0362	0.0353	5.39
Dra f_{nw} = 1	0.704	10.48	5.329	5.03	0.2020	0.0000	5.29
Imb f_{nw} = 0.95	0.655	6.97	8.765	10.99	0.1167	0.0060	12.35
Imb f_{nw} = 0.5	0.538	1.85	17.279	5.22	0.0311	0.0304	5.51
Imb f_{nw} = 0	0.469	3.33	11.722	4.65	0.0000	0.0895	4.88

Table 4: Tabulated experimental and simulated core averaged saturations and relative permeabilities for core 1, along with relative errors.

Fractional flow	S_{nw} exp [-]	S_{nw} sim [-]	S_{nw} rel error [%]	k_{rnw} exp [-]	k_{rnw} sim [-]	k_{rnw} rel error [%]	k_{rw} exp [-]	k_{rw} sim [-]	k_{rw} rel error [%]
Dra f_{nw} = 0.05	0.328	0.327	0.37	0.0058	0.0057	3.21	0.1109	0.1100	0.79
Dra f_{nw} = 1	0.661	0.690	-4.45	0.1226	0.1351	-10.26	0.0000	0.0000	0.00
Imb f_{nw} = 0.95	0.643	0.625	2.85	0.0997	0.0754	24.42	0.0054	0.0040	25.78
Imb f_{nw} = 0.5	0.487	0.532	-9.26	0.0198	0.0259	-30.97	0.0299	0.0258	13.59
Imb f_{nw} = 0	0.362	0.374	-3.35	0.0000	0.0000	0.00	0.1148	0.1498	-30.49

Table 5: Tabulated experimental and simulated core averaged saturations and relative permeabilities for core 2, along with relative errors.

Fractional flow	S_{nw} exp [-]	S_{nw} sim [-]	S_{nw} rel error [%]	k_{rnw} exp [-]	k_{rnw} sim [-]	k_{rww} rel error [%]	k_{rw} exp [-]	k_{rw} sim [-]	k_{rw} rel error [%]
Dra f_{nw} = 0.05	0.333	0.326	1.94	0.0075	0.0071	5.11	0.1386	0.1348	2.67
Dra f_{nw} = 0.5	0.452	0.473	-4.66	0.0362	0.0392	-8.31	0.0353	0.0388	-9.83
Dra f_{nw} = 1	0.704	0.725	-3.00	0.2020	0.2212	-9.49	0.0000	0.0000	0.00
Imb f_{nw} = 0.95	0.655	0.642	1.96	0.1167	0.0954	18.26	0.0060	0.0050	16.79
Imb f_{nw} = 0.5	0.538	0.559	-3.89	0.0311	0.0247	20.83	0.0304	0.0243	20.13
Imb f_{nw} = 0	0.469	0.438	6.53	0.0000	0.0000	0.00	0.0895	0.0961	-7.27

References

[1] J. Bear, *Dynamics of Fluids in Porous Media*. Dover Publications Inc., 1989.

[2] M. Walsh and L. W. Lake, *A Generalized Approach To Primary Hydrocarbon Recovery Of Petroleum Exploration & Production*. Elsevier Science, 2003.

[3] D. K. Todd, *Groundwater Hydrology*. John Wiley & Sons, 2005.

[4] M. O. Schwartz, "Modelling groundwater contamination above the asse 2 medium-level nuclear waste repository, germany," *Environmental Earth Sciences*, vol. 59, pp. 277–286, jan 2009.

[5] S. Finsterle, E. L. Sonnenthal, and N. Spycher, "Advances in subsurface modeling using the TOUGH suite of simulators," *Computers & Geosciences*, vol. 65, pp. 2–12, apr 2014.

[6] S. Krevor, M. J. Blunt, S. M. Benson, C. H. Pentland, C. Reynolds, A. Al-Menhali, and B. Niu, "Capillary trapping for geologic carbon dioxide storage – from pore scale physics to field scale implications," *International Journal of Greenhouse Gas Control*, vol. 40, pp. 221–237, sep 2015.

[7] C. Arns, M. Knackstedt, and N. Martys, "Cross-property correlations and permeability estimation in sandstone," *Physical Review E*, vol. 72, no. 4, 2005.

[8] R. Hilfer and A. Lemmer, "Differential porosimetry and permeametry for random porous media," *Physical Review E*, vol. 92, no. 1, 2015.

[9] D. Zhang, R. Zhang, S. Chen, and W. Soll, "Pore scale study of flow in porous media: Scale dependency, REV, and statistical REV," *Geophysical Research Letters*, vol. 27, no. 8, pp. 1195–1198, 2000.

[10] R. Al-Raoush and A. Papadopoulos, "Representative elementary volume analysis of porous media using x-ray computed tomography," *Powder Technology*, vol. 200, no. 1-2, pp. 69–77, 2010.

[11] R. Armstrong, A. Georgiadis, H. Ott, D. Klemin, and S. Berg, "Critical capillary number: Desaturation studied with fast X-ray computed microtomography," *Geophysical Research Letters*, vol. 41, pp. 55–60, 2014.

[12] C. Land, "Calculation of imbibition relative permeability for two- and three-phase flow from rock properties," *Society of Petroleum Engineers Journal*, pp. 149–156, 1968.

[13] M. Hassanizadeh and W. G. Gray, "General conservation equations for multi-phase systems: 3. constitutive theory for porous media flow," *Advances in Water Resources*, vol. 3, no. 1, pp. 25–40, 1980.

[14] P. C. Reeves and M. A. Celia, "A functional relationship between capillary pressure, saturation, and interfacial area as revealed by a pore-scale network model," *Water Resources Research*, vol. 32, pp. 2345–2358, aug 1996.

[15] J. E. McClure, M. A. Berrill, W. G. Gray, and C. T. Miller, "Influence of phase connectivity on the relationship among capillary pressure, fluid saturation, and interfacial area in two-fluid-phase porous medium systems," *Physical Review E*, vol. 94, no. 3, 2016.

[16] M. Shook, D. Li, and L. Lake, "Scaling immiscible flow through permeable media by inspectional analysis," *In Situ*, vol. 16, no. 4, pp. 311–349, 1992.

[17] P. Ringrose, K. Sorbie, P. Corbett, and J. Jensen, "Immiscible flow behaviour in laminated and cross-bedded sandstones," *Journal of Petroleum Science and Engineering*, vol. 9, pp. 103–124, 1993.

[18] P. Ringrose and P. Corbett, "Controls on two-phase fluid flow in heterogeneous sandstones," *Geological Society, London, Special Publications*, vol. 78, pp. 141–150, 1994.

[19] D. Zhou, F. Fayers, and F. Orr Jr, "Scaling of multiphase flow in simple heterogeneous porous media," in *56th Annual Fall Technical Conference and Exhibition of the Society of Petroleum Engineers of AIME, San Antonio, Texas, October 5-7, 1981*, no. SPE 10109, 1981.

[20] C. Reynolds, "Two-phase flow behaviour and relative permeability between CO_2 and brine in sandstones at the pore and core scales," 2016.

[21] C. A. Reynolds, M. J. Blunt, and S. Krevor, "Multiphase flow characteristics of heterogeneous rocks from CO2 storage reservoirs in the united kingdom," *Water Resources Research*, vol. 54, no. 2, pp. 729–745, 2018.

[22] S. J. Jackson, S. Agada, C. A. Reynolds, and S. Krevor, "Characterizing drainage multiphase flow in heterogeneous sandstones," *Water Resources Research*, vol. 54, no. 4, pp. 3139–3161, 2018.

[23] M. J. Blunt, B. Bijeljic, H. Dong, O. Gharbi, S. Iglauer, P. Mostaghimi, A. Paluszny, and C. Pentland, "Pore-scale imaging and modelling," *Advances in Water Resources*, vol. 51, no. 197, 2013.

[24] Y. Gao, Q. Lin, B. Bijeljic, and M. J. Blunt, "X-ray microtomography of intermittency in multiphase flow at steady state using a differential imaging method," *Water Resources Research*, vol. 53, no. 12, pp. 10274–10292, 2017.

[25] Q. Lin, B. Bijeljic, R. Pini, M. J. Blunt, and S. Krevor, "Imaging and measurement of pore-scale interfacial curvature to determine capillary pressure simultaneously with relative permeability," *Water Resources Research*, vol. 54, no. 9, pp. 7046–7060, 2018.

[26] A. Peksa, K.-A. Wolf, and P. Zitha, "Bentheimer sandstone revisited for experimental purposes," *Marine and Petroleum Geology*, vol. 67, pp. 701–719, 2015.

[27] M. Andrew, B. Bijeljic, and M. J. Blunt, "Pore-scale contact angle measurements at reservoir conditions using x-ray microtomography," *Advances in Water Resources*, vol. 68, pp. 24–31, 2014.

[28] K. Singh, B. Bijeljic, and M. J. Blunt, "Imaging of oil layers, curvature and contact angle in a mixed-wet and a water-wet carbonate rock," *Water Resources Research*, vol. 52, no. 3, pp. 1716–1728, 2016.

[29] M. Halisch, "The rev challenge - estimating representative elementary volumes and porous rock inhomogeneity from high resolution micro-CT data sets," in *International Symposium of the Society of Core Analysts SCA2013-069*, 2013.

[30] A. L. Herring, E. J. Harper, L. Andersson, A. Sheppard, B. K. Bay, and D. Wildenschild, "Effect of fluid topology on residual nonwetting phase trapping: Implications for geologic CO2 sequestration," *Advances in Water Resources*, vol. 62, pp. 47–58, 2013.

[31] S. Schlüter, S. Berg, M. Rücker, R. T. Armstrong, H.-J. Vogel, R. Hilfer, and D. Wildenschild, "Pore-scale displacement mechanisms as a source of hysteresis for two-phase flow in porous media," *Water Resources Research*, vol. 52, no. 3, pp. 2194–2205, 2016.

[32] K. Singh, H. Menke, M. Andrew, Q. Lin, C. Rau, M. J. Blunt, and B. Bijeljic, "Dynamics of snap-off and pore-filling events during two-phase fluid flow in permeable media," *Scientic Reports*, vol. 7, no. 5192, 2017.

[33] C. McPhee, J. Reed, and I. Zubizarreta, *Core Analysis: A best practice guide*, vol. 64. 2015.

[34] A. Georgiadis, G. Maitland, J. P. M. Trusler, and A. Bismarck, "Interfacial tension measurements of the (h2o −− n-decane −− co_2) ternary system at elevated pressures and temperatures," *Journal of Chemical & Engineering Data*, vol. 56, no. 12, pp. 4900–4908, 2011.

[35] R. Aveyard and S. M. Saleem, "Interfacial tensions at alkane-aqueous electrolyte interfaces," *Journal of the Chemical Society, Faraday Transactions 1: Physical Chemistry in Condensed Phases*, vol. 72, no. 0, p. 1609, 1976.

[36] D. E. Goldsack and R. Franchetto, "The viscosity of concentrated electrolyte solutions. i. concentration dependence at fixed temperature," *Canadian Journal of Chemistry*, vol. 55, no. 6, pp. 1062–1072, 1977.

[37] P. Linstrom, "Nist chemistry webbook, nist standard reference database 69," 1997.

[38] S. A. Ghafri, G. C. Maitland, and J. P. M. Trusler, "Densities of aqueous MgCl2(aq), CaCl2(aq), KI(aq), NaCl(aq), KCl(aq), AlCl3(aq), and (0.964 NaCl + 0.136 KCl)(aq) at temperatures between (283 and 472) k, pressures up to 68.5 MPa, and molalities up to 6 mol/kg," *Journal of Chemical & Engineering Data*, vol. 57, no. 4, pp. 1288–1304, 2012.

[39] G. Virnovsky, H. Friis, and A. Lohne, "A steady-state upscaling approach for immiscible two-phase flow," *Transport in Porous Media*, vol. 54, pp. 167–192, 2004.

[40] R. Pini and S. Benson, "Characterization and scaling of mesoscale heterogeneities in sandstones," *Geophysical Research Letters*, vol. 40, pp. 3903–3908, 2013.

[41] S. Berg, M. Rucker, H. Ott, A. Georgiadis, F. E. H. van der Linde, M. Kersten, R. T. Armstrong, S. de With, J. Becker, and A. Wiegmann, "Connected pathway relative permeability from pore-scale imaging of imbibition," *Advances in Water Resources*, vol. 90, no. 24, 2016.

[42] C. A. Reynolds, H. Menke, M. Andrew, M. J. Blunt, and S. Krevor, "Dynamic fluid connectivity during steady-state multiphase flow in a sandstone," *Proceedings of the National Academy of Sciences*, vol. 114, no. 31, pp. 8187–8192, 2017.

[43] C. Spurin, S. Krevor, B. Bijeljic, M. Blunt, and T. Bultreys, "Intermittent fluid connectivity during two-phase flow in a heterogeneous carbonate rock," *In press, Physical Review E*, 2019.

[44] C. Spurin, T. Bultreys, B. Bijeljic, M. Blunt, and S. Krevor, "Mechanisms controlling fluid break-up and reconnection during two-phase flow in porous media," *In press, Physical Review E*, 2019.

[45] M. Rücker, S. Berg, R. T. Armstrong, A. Georgiadis, H. Ott, A. Schwing, R. Neiteler, N. Brussee, A. Makurat, L. Leu, M. Wolf, F. Khan, F. Enzmann, and M. Kersten, "From connected pathway flow to ganglion dynamics," *Geophysical Research Letters*, vol. 42, no. 10, pp. 3888–3894, 2015.

[46] Q. Lin, B. Bijeljic, S. Berg, R. Pini, M. J. Blunt, and S. Krevor, "Minimal surfaces in porous media: Pore-scale imaging of multiphase flow in an altered-wettability bentheimer sandstone," *Physical Review E*, vol. 99, jun 2019.

[47] A. Buades, B. Coll, and J.-M. Morel, "Nonlocal image and movie denoising," *International Journal of Computer Vision*, vol. 76, no. 2, pp. 123–139, 2007.

[48] Q. Lin, Y. Al-Khulaifi, M. J. Blunt, and B. Bijeljic, "Quantification of sub-resolution porosity in carbonate rocks by applying high-salinity contrast brine using x-ray microtomography differential imaging," *Advances in Water Resources*, vol. 96, pp. 306–322, 2016.

[49] Q. Lin, B. Bijeljic, H. Rieke, and M. J. Blunt, "Visualization and quantification of capillary drainage in the pore space of laminated sandstone by a porous plate method using differential imaging x-ray microtomography," *Water Resources Research*, vol. 53, no. 8, pp. 7457–7468, 2017.

[50] M. Andrew, B. Bijeljic, and M. J. Blunt, "Pore-by-pore capillary pressure measurements using x-ray microtomography at reservoir conditions: Curvature, snap-off, and remobilization of residual CO2," *Water Resources Research*, vol. 50, no. 11, pp. 8760–8774, 2014.

[51] A. Jones, A. C, A. Sheppard, D. Hutmacher, B. Milthorpe, and M. Knackstedt, "Assessment of bone ingrowth into porous biomaterials using MICRO-CT," *Biomaterials*, vol. 28, no. 15, pp. 2491–2504, 2007.

[52] R. T. Armstrong, M. L. Porter, and D. Wildenschild, "Linking pore-scale interfacial curvature to column-scale capillary pressure," *Advances in Water Resources*, vol. 46, pp. 55–62, 2012.

[53] T. Li, S. Schlüter, M. I. Dragila, and D. Wildenschild, "An improved method for estimating capillary pressure from 3d microtomography images and its application to the study of disconnected nonwetting phase," *Advances in Water Resources*, vol. 114, pp. 249–260, 2018.

[54] R. Armstrong, C. Pentland, S. Berg, J. Hummel, D. Lichau, and L. Bernard, "Estimation of curvature from micro-ct liquid-liquid displacement studies with pore scale resolution," in *International Symposium of the Society of Core Analysts SCA2012-55*, 2012.

[55] C. Garing, J. A. de Chalendar, M. Voltolini, J. B. Ajo-Franklin, and S. M. Benson, "Pore-scale capillary pressure analysis using multi-scale x-ray micromotography," *Advances in Water Resources*, vol. 104, pp. 223–241, 2017.

[56] A. L. Herring, J. Middleton, R. Walsh, A. Kingston, and A. Sheppard, "Flow rate impacts on capillary pressure and interface curvature of connected and disconnected fluid phases during multiphase flow in sandstone," *Advances in Water Resources*, vol. 107, pp. 460–469, 2017.

[57] M. Muskat and M. W. Meres, "The flow of heterogeneous fluids through porous media," *Physics*, vol. 7, no. 9, pp. 346–363, 1936.

[58] J. Niessner, S. Berg, and S. M. Hassanizadeh, "Comparison of two-phase darcy's law with a thermodynamically consistent approach," *Transport in Porous Media*, vol. 88, no. 1, pp. 133–148, 2011.

[59] S. Whitaker, "Flow in porous media II: The governing equations for immiscible, two-phase flow," *Transport in Porous Media*, vol. 1, no. 2, pp. 105–125, 1986.

[60] A. Bourgeat, "Two-phase flow," in *Homogenization and Porous Media. Interdisciplinary Applied Mathematics, vol 6.*, pp. 95–127, Springer New York, 1997.

[61] M. J. Blunt, *Multiphase Flow in Permeable Media: A Pore-Scale Perspective*. Cambridge University Press, 2017.

[62] J.-C. Perrin, M. Krause, C.-W. Kuo, L. Miljkovic, E. Charoba, and S. M. Benson, "Core-scale experimental study of relative permeability properties of CO2 and brine in reservoir rocks," *Energy Procedia*, vol. 1, no. 1, pp. 3515–3522, 2009.

[63] R. T. Armstrong, J. E. McClure, M. A. Berrill, M. Rücker, S. Schlüter, and S. Berg, "Beyond darcy's law: The role of phase topology and ganglion dynamics for two-fluid flow," *Physical Review E*, vol. 94, no. 4, 2016.

[64] M. Oak, "Three-phase relative permeability of water-wet berea," in *SPE/DOE Seventh Symposium on Enhanced Oil Recovery, Tulsa, Oklahoma*, 1980.

[65] D. Picchi and I. Battiato, "Relative permeability scaling from pore-scale flow regimes," *Water Resources Research*, vol. 55, no. 4, pp. 3215–3233, 2019.

[66] R. H. Brooks and A. T. Corey, *Hydraulic properties of porous media*. 1964.

[67] M. R. Razavi, B. Muhunthan, and O. A. Hattamleh, "Representative elementary volume analysis of sands using x-ray computed tomography," *Geotechnical Testing Journal*, vol. 30, no. 3, p. 100164, 2007.

[68] A. Georgiadis, S. Berg, A. Makurat, G. Maitland, and H. Ott, "Pore-scale micro-computed-tomography imaging: Nonwetting-phase cluster-size distribution during drainage and imbibition," *Physical Review E*, vol. 88, sep 2013.

[69] M. S. Costanza-Robinson, B. D. Estabrook, and D. F. Fouhey, "Representative elementary volume estimation for porosity, moisture saturation, and air-water interfacial areas in unsaturated porous media: Data quality implications," *Water Resources Research*, vol. 47, no. 7, 2011.

[70] J. L. Jensen, P. W. M. Corbett, G. E. Pickup, and P. S. Ringrose, "Permeability semivariograms, geological structure, and flow performance," *Mathematical Geology*, vol. 28, no. 4, pp. 419–435, 1996.

[71] P. Ringrose and M. Bentley, *Reservoir Model Design. A Practitioners Guide*. Springer, Dordrecht, 2015.

[72] A. AlRatrout, M. J. Blunt, and B. Bijeljic, "Spatial correlation of contact angle and curvature in pore-space images," *Water Resources Research*, vol. 54, no. 9, pp. 6133–6152, 2018.

[73] N. R. Morrow, "Physics and thermodynamics of capillary action in porous media," *Industrial & Engineering Chemistry*, vol. 62, no. 6, pp. 32–56, 1970.

[74] J. E. McClure, R. T. Armstrong, M. A. Berrill, S. Schlüter, S. Berg, W. G. Gray, and C. T. Miller, "Geometric state function for two-fluid flow in porous media," *Physical Review Fluids*, vol. 3, no. 8, 2018.

[75] E. J. Spiteri, R. Juanes, M. J. Blunt, and F. M. Orr, "A new model of trapping and relative permeability hysteresis for all wettability characteristics," *SPE Journal*, vol. 13, no. 03, pp. 277–288, 2008.

[76] V. Joekar-Niasar, S. M. Hassanizadeh, and A. Leijnse, "Insights into the relationships among capillary pressure, saturation, interfacial area and relative permeability using pore-network modeling," *Transport in Porous Media*, vol. 74, no. 2, pp. 201–219, 2007.

[77] L. J. Pyrak-Nolte, D. D. Nolte, D. Chen, and N. J. Giordano, "Relating capillary pressure to interfacial areas," *Water Resources Research*, vol. 44, no. 6, 2008.

[78] M. L. Porter, D. Wildenschild, G. Grant, and J. I. Gerhard, "Measurement and prediction of the relationship between capillary pressure, saturation, and interfacial area in a NAPL-water-glass bead system," *Water Resources Research*, vol. 46, no. 8, 2010.

[79] R. T. Armstrong, J. E. McClure, V. Robins, Z. Liu, C. H. Arns, S. Schlüter, and S. Berg, "Porous media characterization using minkowski functionals: Theories, applications and future directions," *Transport in Porous Media*, 2018.

[80] D. A. Klain, "A short proof of hadwiger's characterization theorem," *Mathematika*, vol. 42, no. 2, pp. 329–339, 1995.

[81] S. M. Hassanizadeh and W. G. Gray, "Toward an improved description of the physics of two-phase flow," *Advances in Water Resources*, vol. 16, no. 1, pp. 53–67, 1993.

[82] W. G. Gray and C. T. Miller, "Thermodynamically constrained averaging theory approach for modeling flow and transport phenomena in porous medium systems: 1. motivation and overview," *Advances in Water Resources*, vol. 28, no. 2, pp. 161–180, 2005.

[83] M. Honarpour, A. Cullick, N. Saad, and N. Humphreys, "Effect of rock heterogeneity on relative permeability: Implications for scaleup," *Journal of Petroleum Technology*, vol. 47, no. 11, pp. 980–986, 1995.

[84] R. Pini, S. Krevor, and S. Benson, "Capillary pressure and heterogeneity for the CO_2/water system in sandstone rocks at reservoir conditions," *Advances in Water Resources*, vol. 38, pp. 48–59, 2012.

[85] M. Krause, S. Krevor, and S. Benson, "A procedure for the accurate determination of sub-core scale permeability distributions with error quantification," *Transport in Porous Media*, vol. 93, no. 3, pp. 565–588, 2013.

[86] M. Krause and S. Benson, "Accurate determination of characteristic relative permeability curves," *Advances in Water Resources*, vol. 83, pp. 376–388, 2015.

[87] L. Durlofsky, "Numerical calculation of equivalent grid block permeability tensors for heterogeneous porous media," *Water Resources Research*, vol. 27, no. 5, pp. 699–708, 1991.

[88] G. Dagan, A. Fiori, and I. Jankovic, "Upscaling of flow in heterogeneous porous formations: Critical examination and issues of principle," *Advances in Water Resources*, vol. 51, pp. 67–85, 2013.

[89] S. J. Jackson and S. Krevor, "Characterization of hysteretic multiphase flow from the mm to m scale in heterogeneous rocks," *E3S Web of Conferences*, vol. 89, p. 02001, 2019.

[90] F. M. Carlson, "Simulation of relative permeability hysteresis to the nonwetting phase," in *SPE Annual Technical Conference and Exhibition*, Society of Petroleum Engineers, 1981.

[91] G. R. Jerauld, "Prudhoe bay gas/oil relative permeability," *SPE Reservoir Engineering*, vol. 12, no. 01, pp. 66–73, 1997.

[92] J. E. Killough, "Reservoir simulation with history-dependent saturation functions," *Society of Petroleum Engineers Journal*, pp. 37–48, 1976.

[93] P. Øren, L. Ruspini, M. Saadatfar, R. Sok, M. Knackstedt, and A. Herring, "In-situ pore-scale imaging and image-based modelling of capillary trapping for geological storage of CO2," *International Journal of Greenhouse Gas Control*, vol. 87, pp. 34–43, 2019.

[94] S. Shi, H. Belhaj, and A. Bera, "Capillary pressure and relative permeability correlations for transition zones of carbonate reservoirs," *Journal of Petroleum Exploration and Production Technology*, vol. 8, no. 3, pp. 767–784, 2017.

[95] M. Akbarabadi and M. Piri, "Relative permeability hysteresis and capillary trapping characteristics of supercritical CO_2/brine systems: an experimental study at reservoir conditions," *Advances in Water Resources*, vol. 52, pp. 190–206, 2012.

[96] R. Pini and S. M. Benson, "Capillary pressure heterogeneity and hysteresis for the supercritical CO_2/water system in a sandstone," *Advances in Water Resources*, vol. 108, pp. 277–292, 2017.

[97] J. Kleppe, P. Delaplace, R. Lenormand, G. Hamon, and E. Chaput, "Representation of capillary pressure hysteresis in reservoir simulation," in *SPE Annual Technical Conference and Exhibition*, Society of Petroleum Engineers, 1997.

[98] B. Raeesi, N. R. Morrow, and G. Mason, "Capillary pressure hysteresis behavior of three sandstones measured with a multistep outflow–inflow apparatus," *Vadose Zone Journal*, vol. 13, no. 3, p. 0, 2014.

[99] N. Bech and P. Frykman, "Trapping of buoyancy-driven CO2 during imbibition," *International Journal of Greenhouse Gas Control*, vol. 78, pp. 48–61, 2018.

[100] S. C. M. Krevor, R. Pini, B. Li, and S. M. Benson, "Capillary heterogeneity trapping of CO_2 in a sandstone rock at reservoir conditions," *Geophysical Research Letters*, vol. 38, p. L15401, 2011.

[101] S. Bakke and P.-E. Øren, "3-d pore-scale modelling of sandstones and flow simulations in the pore networks," *SPE Journal*, vol. 2, no. 02, pp. 136–149, 1997.

[102] A. P. Jivkov, C. Hollis, F. Etiese, S. A. McDonald, and P. J. Withers, "A novel architecture for pore network modelling with applications to permeability of porous media," *Journal of Hydrology*, vol. 486, pp. 246–258, 2013.

[103] C. van der Land, R. Wood, K. Wu, M. I. J. van Dijke, Z. Jiang, P. W. M. Corbett, and G. Couples, "Modelling the permeability evolution of carbonate rocks," *Marine and Petroleum Geology*, vol. 48, pp. 1–7, 2013.

[104] A. Q. Raeini, M. J. Blunt, and B. Bijeljic, "Direct simulations of two-phase flow on micro-CT images of porous media and upscaling of pore-scale forces," *Advances in Water Resources*, vol. 74, pp. 116–126, 2014.

[105] H. Dong and M. J. Blunt, "Pore-network extraction from micro-computerized-tomography images," *Physical Review E*, vol. 80, no. 3, 2009.

[106] M. C. Leverett, "Capillary behavior in porous solids," *Transactions of the AIME*, vol. 142, no. 01, pp. 152–169, 1941.

[107] P. W. M. Corbett, P. S. Ringrose, J. L. Jensen, and K. S. Sorbie, "Laminated clastic reservoirs: The interplay of capillary pressure and sedimentary architecture," in *67th Annual Technical Conference and Exhibition of the Society of Petroleum Engineers, Washington D.C., October 4-7, 1992*, no. SPE 24699, 1992.

[108] K. Nordahl, P. S. Ringrose, and R. Wen, "Petrophysical characterization of a heterolithic tidal reservoir interval using a process-based modelling tool," *Petroleum Geoscience*, vol. 11, pp. 17–28, 2005.

[109] H. Fossen, R. A. Schultz, Z. K. Shipton, and K. Mair, "Deformation bands in sandstone: a review," *Journal of the Geological Society*, vol. 164, no. 4, pp. 755–769, 2007.

[110] M. Chaouche, N. Rakotomalala, D. Salin, and Y. C. Yortsos, "Capillary effects in immiscible flows in heterogeneous porous media," *Europhysics Letters (EPL)*, vol. 21, no. 1, pp. 19–24, 1993.

[111] M. Chaouche, N. Rakotomalala, D. Salin, B. Xu, and Y. Yortsos, "Capillary effects in drainage in heterogeneous porous media: continuum modelling, experiments and pore network simulations," *Chemical Engineering Science*, vol. 49, no. 15, pp. 2447–2466, 1994.

[112] J. Fernandes, C. Appoloni, and C. Fernandes, "Determination of the representative elementary volume for the study of sandstones and siltstones by X-Ray microtomography," *Materials Research*, vol. 15, no. 4, pp. 662–670, 2012.

[113] A. Herring, F. Gilby, Z. Li, J. McClure, M. Turner, J. Veldkamp, L. Beeching, and A. Sheppard, "Observations of nonwetting phase snap-off during drainage," *Advances in Water Resources*, vol. 121, pp. 32–43, 2018.

[114] M. Andrew, H. Menke, M. J. Blunt, and B. Bijeljic, "The imaging of dynamic multiphase fluid flow using synchrotron-based x-ray microtomography at reservoir conditions," *Transport in Porous Media*, vol. 110, no. 1, 2015.

[115] R. Lenormand, C. Zarcone, and A. Sarr, "Mechanisms of the displacement of one fluid by another in a network of capillary ducts," *Journal of Fluid Mechanics*, vol. 135, no. -1, p. 337, 1983.

[116] L. F. Ruppert, R. Sakurovs, T. P. Blach, L. He, Y. B. Melnichenko, D. F. R. Mildner, and L. Alcantar-Lopez, "A USANS/SANS study of the accessibility of pores in the barnett shale to methane and water," *Energy & Fuels*, vol. 27, no. 2, pp. 772–779, 2013.

[117] W. B. Haines, "Studies in the physical properties of soil. v. the hysteresis effect in capillary properties, and the modes of moisture distribution associated therewith," *The Journal of Agricultural Science*, vol. 20, no. 1, pp. 97–116, 1930.

[118] S. Berg, H. Ott, S. A. Klapp, A. Schwing, R. Neiteler, N. Brussee, A. Makurat, L. Leu, F. Enzmann, J.-O. Schwarz, M. Kersten, S. Irvine, and M. Stampanoni, "Real-time 3d imaging of haines jumps in porous media flow," *Proceedings of the National Academy of Sciences*, vol. 110, no. 3755, 2013.

[119] M. Tuller and D. Or, "Hydraulic conductivity of variably saturated porous media: Film and corner flow in angular pore space," *Water Resources Research*, vol. 37, no. 5, pp. 1257–1276, 2001.

[120] H. Ni, M. Boon, C. Garing, and S. M. Benson, "Predicting CO2 residual trapping ability based on experimental petrophysical properties for different sandstone types," *International Journal of Greenhouse Gas Control*, vol. 86, pp. 158–176, 2019.

[121] L. Trevisan, R. Pini, A. C. nd J.T. Birkholzer, Q. Zhou, A. González-Nicolás, and T. Illangasekare, "Imaging and quantification of spreading and trapping of carbon dioxide in saline aquifers using meter-scale laboratory experiments," *Water Resources Research*, vol. 53, no. 1, pp. 485–502, 2017.

[122] W. G. Anderson, "Wettability literature survey part 5: The effects of wettability on relative permeability," *Journal of Petroleum Technology*, vol. 39, no. 11, pp. 1453–1468, 1987.

[123] T. K. Tokunaga, J. Wan, J.-W. Jung, T. W. Kim, Y. Kim, and W. Dong, "Capillary pressure and saturation relations for supercritical CO2 and brine in sand: High-pressure pc (sw) controller/meter measurements and capillary scaling predictions," *Water Resources Research*, vol. 49, no. 8, pp. 4566–4579, 2013.

[124] C. A. Reynolds and S. C. Krevor, "Characterizing flow behaviour for gas injection: Relative permeability of CO_2-brine and N_2-water in heterogeneous rocks," *Water Resources Research*, vol. 51, no. 12, pp. 9464–9489, 2015.

[125] A. A. Dietrich Stauffer, *Introduction To Percolation Theory*. Taylor & Francis Ltd, 1994.

[126] M. Blunt, M. J. King, and H. Scher, "Simulation and theory of two-phase flow in porous media," *Physical Review A*, vol. 46, no. 12, pp. 7680–7699, 1992.

[127] S. A. H. Hejazi, S. Shah, and R. Pini, "Dynamic measurements of drainage capillary pressure curves in carbonate rocks," *Chemical Engineering Science*, vol. 200, pp. 268–284, jun 2019.

[128] H. A. Nooruddin and M. J. Blunt, "Large-scale invasion percolation with trapping for upscaling capillary-controlled darcy-scale flow," *Transport in Porous Media*, vol. 121, pp. 479–506, nov 2017.

[129] E. Saadatpoor, S. L. Bryant, and K. Sepehrnoori, "New trapping mechanism in carbon sequestration," *Transport in Porous Media*, vol. 82, pp. 3–17, 2010.